Chapter 5

Results and Discussion

This chapter presents the results of this work. The most important results that followed from the respective studies will be discussed as the following. First, growth of $CuIn_{1-x}Ga_xSe_2$ polycrystalline films with various composition (x) using two-stage process with *in situ* monitoring technique will be discussed. The growth and characterization of $CuGaSe_2$ polycrystalline films using both two-stage and three-stage growth processes are presented. The $Cu(In,Ga)Se_2$ solar cell device performances are also discussed in this chapter.

5.1 Growth of $CuIn_{1-x}Ga_xSe_2$ Thin Films with Variation of x Using Two-stage Growth Process

5.1.1 *in situ* Signals and Film Characterization

In this section, the $CuIn_{1-x}Ga_xSe_2$ thin films were grown by two-stage process with a composition range of $0 \leq x \leq 1$, where $x = \frac{[Ga]}{[In]+[Ga]}$ corresponding to a band gap range of $1.0eV < E_g < 1.7eV$. The temperature profiles of elemental sources and substrates are shown in Fig. 5.1. The Ga and In fluxes necessary for producing films at the desired level of Ga incorporation (taken 6 levels: 0%, 35%, 50%, 70%, and 100% Ga) were determined by the calculation described in Chapter 4. The fabrication parameters of the $CuIn_{1-x}Ga_xSe_2$ films with variation of x were as the following: final

thickness was about 2-2.3 μm, $\frac{[Cu]}{[In]+[Ga]}$ (y, or Cu content) at the end of the first stage ≈ 1.3, final y ≈ 0.9, substrate temperature was kept constant at 520°C. After deposition, the sample was cooled down slowly (20°C/min) while Se flux was maintained until the surface temperature have fallen down to 320°C.

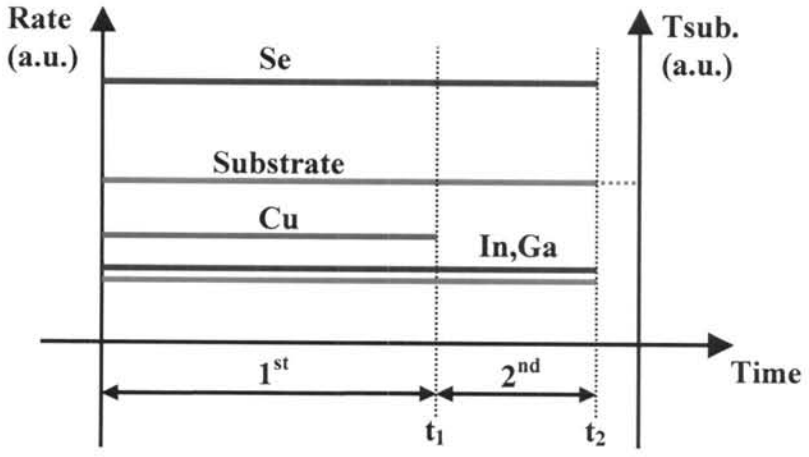

Figure 5.1: Temperature profiles of elemental sources for two-stage growth process.

After $CuIn_{1-x}Ga_xSe_2$ fabrication process, the thickness of these films was measured using Dektak profiler measurements. These films were also characterized by X-ray diffraction (XRD), scanning electron microscopy (SEM), optical transmission and reflection measurement, and the composition was evaluated using energy dispersive X-ray spectroscopy (EDS).

Figure 5.2 shows the typical *in situ* monitoring signals as a function of the process time during the two-stage growth process. T_{pyro} signal shows the amplitude of oscillation decreasing with the deposition time. This is brought about by the decrease of the transmittance of the IR radiation through the substrate, due to the increasing of the Cu-rich $CuIn_{1-x}Ga_xSe_2$ film thickness and free carrier absorption [62].

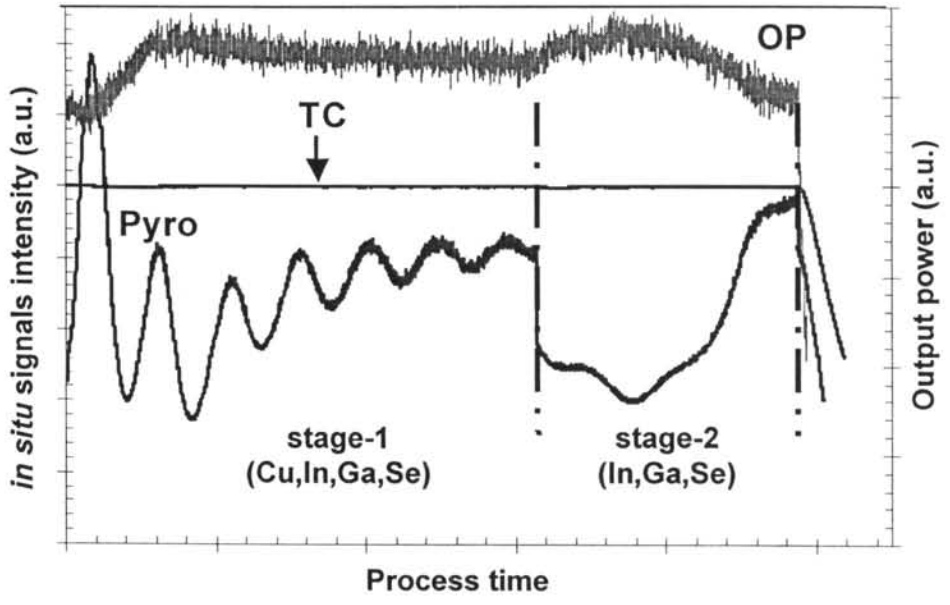

Figure 5.2: Typical profiles of the *in situ* signals; T_{Pyro}, OP, and the substrate temperature (TC) during the two-stage growth process of $CuIn_{1-x}Ga_xSe_2$ films.

Figure 5.3 shows the surface morphologies of some representative $CuIn_{1-x}Ga_xSe_2$ films with a predominant polycrystalline texture. The composition of the films, determined from EDS analysis with ZAF correction, are given in Table 5.1.

Table 5.1: Chemical composition of representative $CuIn_{1-x}Ga_xSe_2$ films

Sample	Cu (at%)	In (at%)	Ga (at%)	[Metal]/[Se]	y ≡ [Cu]/([In]+[Ga])	x ≡ [Ga]/([In]+[Ga])
A	23.72	24.53	0.00	0.93	0.97	0.00
B	22.69	16.56	9.70	0.96	0.86	0.37
C	22.79	12.99	13.80	0.98	0.85	0.52
D	24.04	8.27	18.52	1.03	0.90	0.69
E	24.63	0.00	27.62	1.09	0.89	1.00

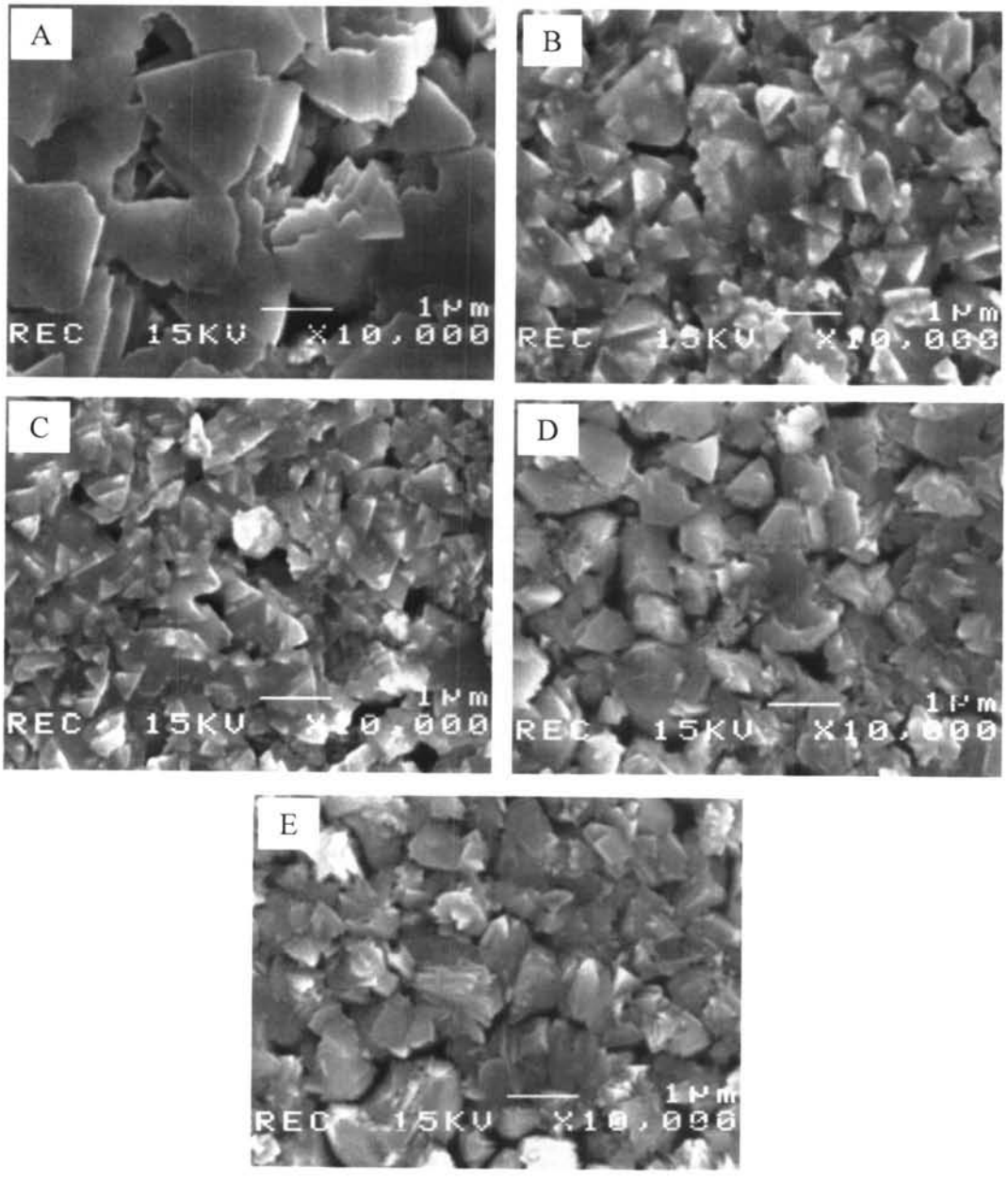

Figure 5.3: SEM micrographs of five representative $CuIn_{1-x}Ga_xSe_2$ films with x ratios of: (A) 0.00; (B) 0.37; (C) 0.52; (D) 0.69 and (E) 1.0.

The final composition of films (y) as shown in Table 5.1 indicated that we can use the *in situ* monitoring technique to detect the end point of the growth process. As described in chapter 4, the transition of signals in the 2nd stage of the process, the T_{pyro} signal increases together with the OP signal decreases. Incidentally, both sharp corners of these two signals occur almost at the same position of the time scale. We attribute these transitions to the point indicating that the $CuIn_{1-x}Ga_xSe_2$ film has been completely transformed to the Cu-poor films. The composition of these $CuIn_{1-x}Ga_xSe_2$ films ended at this point were analyzed by the EDS to be $y \approx 0.9$ as shown in the column of y values in Table 5.1.

5.1.2 Evaluation of Optical Parameters

This section presents the results corresponding to the optical properties of the $CuIn_{1-x}Ga_xSe_2$ thin films depicted in Fig. 5.3. After $CuIn_{1-x}Ga_xSe_2$ growth process, the thicknesses of films were measured by Dektak profiler measurement. In order to determine the band gap (E_g), refractive index (n), and absorption coefficient (α) of the films in this work, optical transmission (T) and reflectance (R) measurements were performed at room temperature with unpolarized light at normal incidence in the wavelength range between 300 and 2600 nm using a double-beam spectrophotometer. The bare SLG was used as a reference sample to determine the total transmission of the $CuIn_{1-x}Ga_xSe_2$ layers.

Figure 5.4 shows the transmittance versus wavelength traces of five representative $Cu(InGa)Se_2$ films with different x ratios. The band edge is shifted towards higher energies as the Ga concentration increases. It may be observed that the fall of T with decreasing wavelength of incident radiation is sharper for $CuIn_{1-x}Ga_xSe_2$ films having lower Ga content and it becomes less sharp for those having higher Ga content. This indicates that in the $CuGaSe_2$ film, the contribution of photon absorption

via states within the energy band gap (probably caused by mechanical defects and/or band tail) is greater than in the $CuIn_{1-x}Ga_xSe_2$ films with lower content of Ga.

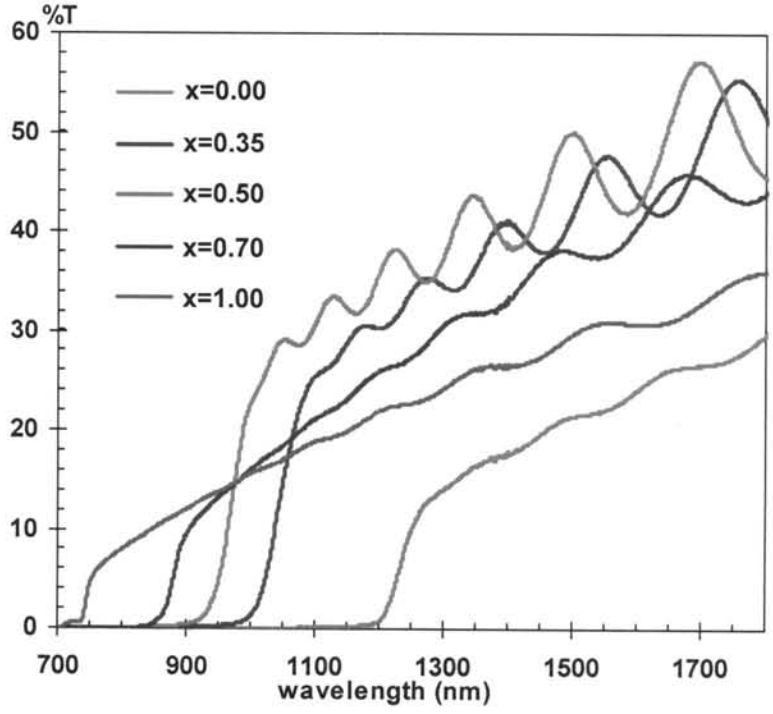

Figure 5.4: Optical transmittance versus wavelength traces for five representative $CuIn_{1-x}Ga_xSe_2$ films having different [Ga]/([In]+[Ga]) ratios. Transmittance spectra of $CuIn_{1-x}Ga_xSe_2$ thin films deposited by MBD with Ga contents of x=0.00, x=0.35, x=0.50, x=0.70, and x=1.00.

P. Guha *et al.* [63] suggested that the less sharp fall of transmittance of high Ga content in $CuIn_{1-x}Ga_xSe_2$ films is due to the existence of copper vacancies (V_{Cu}). The V_{Cu} act as defect states, then often modulate the fall of the transmittance trace because the transitions also occur through the defect states.

Using this information, the refractive index of films with various x can be determined by straightforward calculations from interference fringes in reflection spectrum. The value of thickness of film, d, the location of the interference maxima and minima are related to the real part of the refractive index through expressions [64, 65]:

$$2nd = m\lambda, \tag{5.1}$$

$$d = \frac{\lambda_1 \lambda_2}{2(\lambda_1 n_2 - \lambda_2 n_1)}, \tag{5.2}$$

where n_1, n_2 are the refractive index at λ_1, λ_2, respectively. The interference order m is an integer for maxima and half integer for minima. Table 5.2 shows the example calculation of $CuIn_{1-x}Ga_xSe_2$ film with x = 0.5 which its reflection spectrum is shown in Fig. 5.5.

Table 5.2: The calculation of n at maxima, minima wavelengths of $CuIn_{1-x}Ga_xSe_2$ film with x = 0.50 and thickness of 2.213 μm.

	λ (nm)	n	m (estimated)	m (exact)	d (new) (μm)
maxima	1232.9	2.801	10.2	10	2.2006
	1355.4	2.765	9.2	9	2.2051
	1511.7	2.732	8.1	8	2.2127
	1710.9	2.702	7.15	7	2.2155
	1983.9	2.675	6.1	6	2.2244
minima	1290.2	2.783	9.7	9.5	2.2017
	1428.8	2.749	8.7	8.5	2.2090
	1605.5	2.717	7.6	7.5	2.2157
	1838.8	2.688	6.6	6.5	2.2227
				Average thickness (d_{ave})	2.2104
				Standard deviation	0.0077

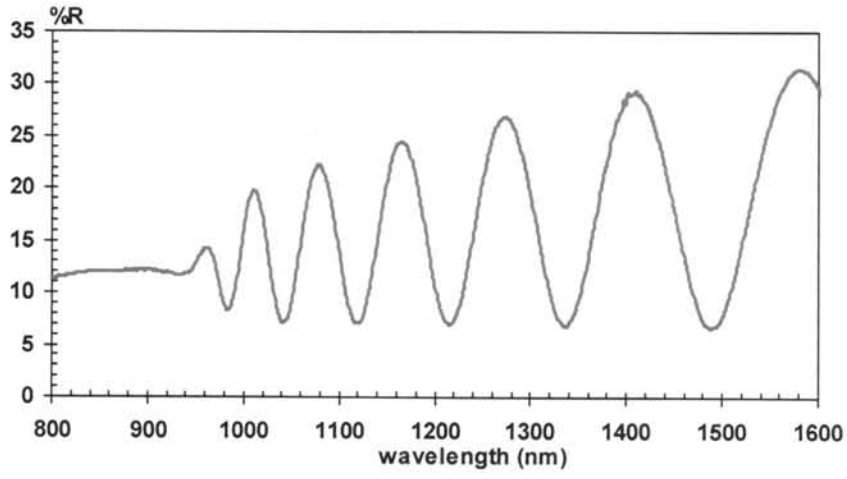

Figure 5.5: Reflection spectrum of $CuIn_{1-x}Ga_xSe_2$ film with x = 0.5.

The n vesus λ curves of all the $CuIn_{1-x}Ga_xSe_2$ samples studied are shown in Fig 5.6. These curves are fitted to a polynomial expression of the form $n=G+B/\lambda^2$ (Cauchy equation), indicating that, in the range of wavelengths studied, the $CuIn_{1-x}Ga_xSe_2$ films present normal dispersion [66]. The constant A and B determined from the fitting are shown in Table. 5.3.

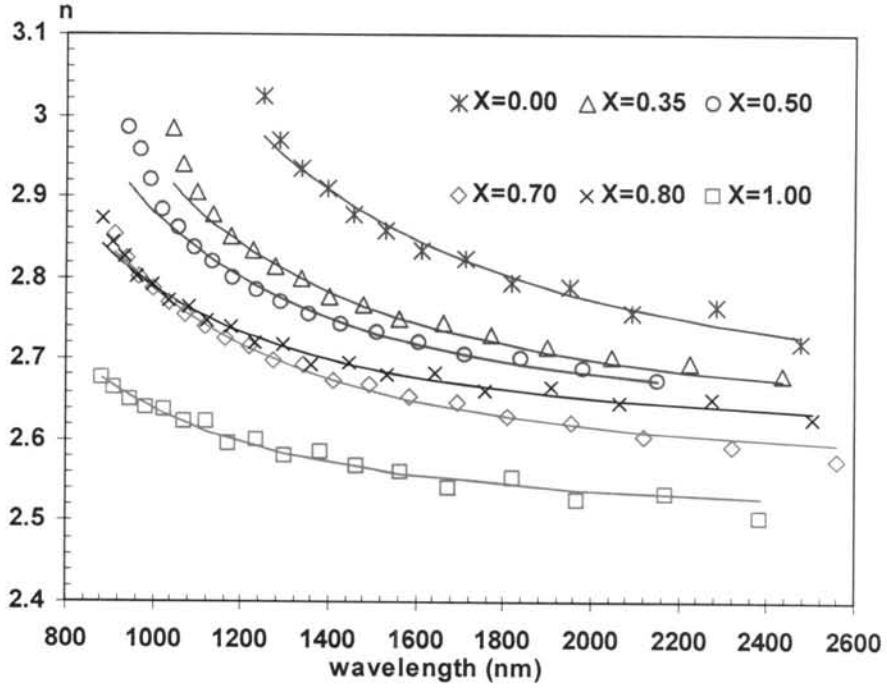

Figure 5.6: Curves of n versus λ, corresponding to $CuIn_{1-x}Ga_xSe_2$ thin film fabricated by MBD with Ga contents of x=0.00, x=0.35, x=0.50, x=0.70, x=0.80, and x=1.00.

Table 5.3: G and B values for $CuIn_{1-x}Ga_xSe_2$ films with Ga contents of x=0.00, x=0.35, x=0.50, x=0.70, x=0.80, and x=1.00.

Ga content	$n= G + (B/\lambda^2)$	
	G	B
0.00	2.645	0.514
0.35	2.62	0.319
0.50	2.615	0.266
0.70	2.559	0.227
0.80	2.606	0.183
1.00	2.504	0.134

The values of the refractive index, n, of the $CuIn_{1-x}Ga_xSe_2$ thin films decrease with the Ga content. The refractive index of the $CuInSe_2$ film is greater than that of the $CuGaSe_2$ film. This behavior seems to be associated with an increase of both the conductivity under illumination and the photo-conductivity of CIS films when their In content increases, taking into account that the refractive index can be expressed by the relation, $n = \frac{4\pi\sigma}{c\alpha}$ [67] and that the absorption coefficient of both materials are similar.

The absorption coefficient was determined from T and R spectra and the film thickness d, using the following equation [68, 69]:

$$\exp(-\alpha d) = \frac{\sqrt{(1-R)^4 + 4T^2R^2} - (1-R)^2}{2TR^2}. \qquad (5.3)$$

Typically, the optical band gap E_g of direct gap semiconductor was determined using the relation [70, 71]

$$\alpha(h\nu) = A(h\nu - E_g)^{1/2}. \qquad (5.4)$$

The optical band gap can be determined from an $(\alpha h\nu)^2$ - $h\nu$ plot where $h\nu$ is the photon energy and G is a constant related to the optical matrix element that depends on the nature of the radiation. In our work, E_g of the $CuIn_{1-x}Ga_xSe_2$ films with $0.00 \leq x \leq 0.80$ can be obtained using this expression. However, the optical absorption spectra of our $CuIn_{1-x}Ga_xSe_2$ film with $x = 1.00$ exhibit peak around the fundamental absorption edge (see Fig 5.7). Thus, the direct band gap energy could not be estimated from typically $(\alpha h\nu)^2$ - $h\nu$ plot. This result implies the contribution of the free exciton (FE) absorption in absorption spectra. Hence, the FE absorption is assumed to have Gaussian profiles taking only ground state (n=1) exciton in determination of E_g. Chichibu *et al.* [32] have reported that the optical absorption spectra of $CuIn_{1-x}Ga_xSe_2$ films did not exhibit FE absorption peak even at 100 K but our results showed that the FE absorption peak of $CuGaSe_2$ films are clearly observed even at room temperature, indicating such high quality of the film.

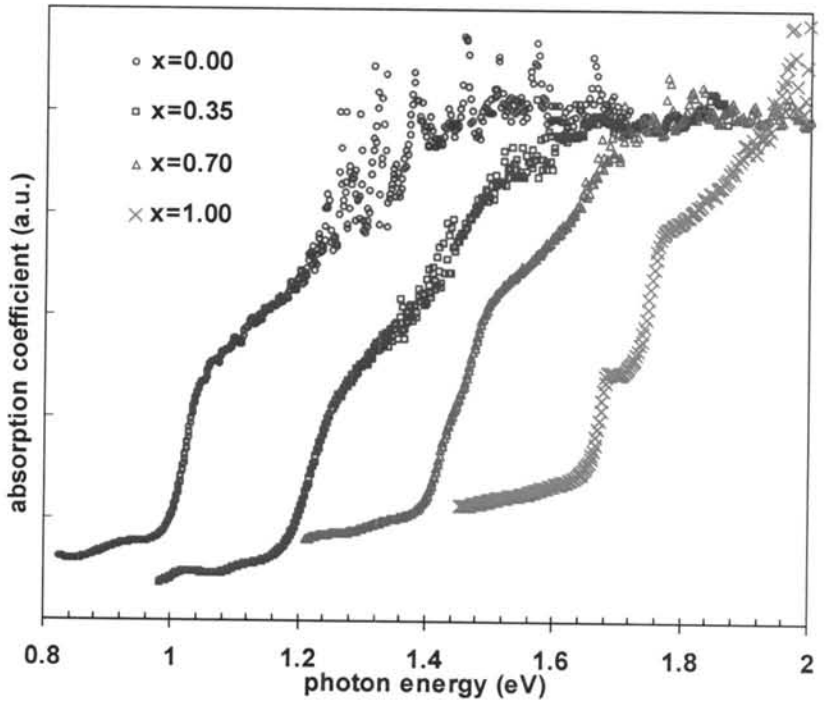

Figure 5.7: Example of absorption spectra of $CuIn_{1-x}Ga_xSe_2$ thin films with x-ratios ranging from 0.00 to 1.00 measured at 300K.

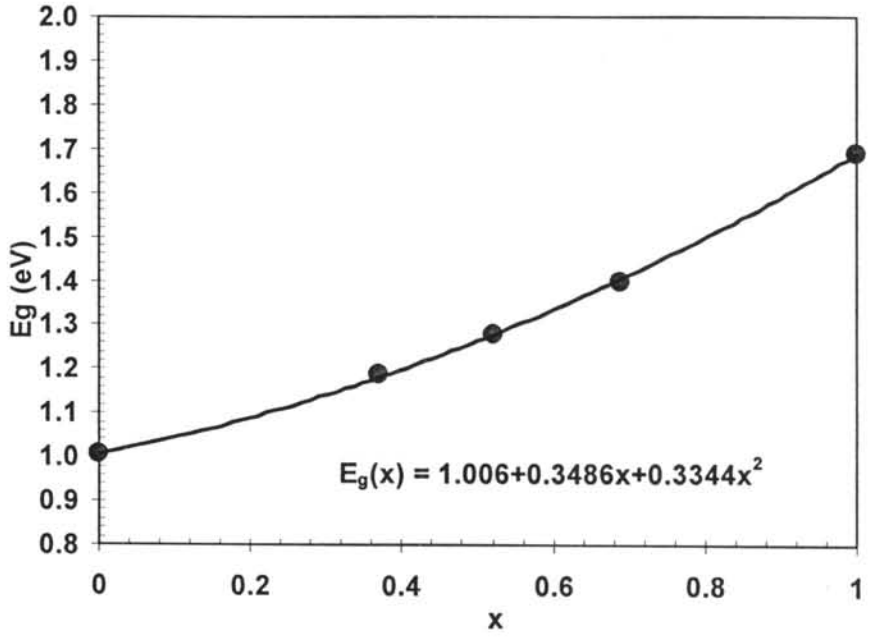

Figure 5.8: Variation of band gap energy (E_g) with x values of $CuIn_{1-x}Ga_xSe_2$ films.

The E_g increase with increasing [Ga]/([In]+[Ga])-ratios is shown in Fig. 5.8. It may be observed that E_g versus x plot shows a bowing behavior which may be expressed as [72]

$$E_g^{CIGS} = E_g^{CIS}x + E_g^{CGS}(1-x) - bx(1-x), \qquad (5.5)$$

where E_g^{CIS} is the band gap energy of $CuInSe_2$ (x=0), E_g^{CGS} is the band gap energy of $CuGaSe_2$ (x=1), E_g^{CIGS} is the band gap energy of $CuIn_{1-x}Ga_xSe_2$ and b is the bowing parameter. For our $CuIn_{1-x}Ga_xSe_2$ films, the curve fitting of the E_g versus x can be written as

$$E_g(x) = 1.006 + 0.3486x + 0.3344x^2. \qquad (5.6)$$

The bowing parameter, b is ≈ 0.33. For x=1 Eq. 5.6 give E_g=1.69eV which agrees well with the band gap of $CuGaSe_2$ [73]. The bowing parameter obtained in this work is lower than the value of 0.38 reported by NREL [74].

5.2 Evolution of Structural and Morphology of $CuGaSe_2$ Thin Films Grown by MBD Using Two-stage Process

This section describes the investigations of a series of wide band gap $CuGaSe_2$ polycrystalline thin films with variation of [Cu]/[Ga] (or Cu/Ga-ratio) grown by two-stage growth process with *in situ* monitoring technique. The evolution of both the morphology and structural properties of these films is described, and correlations between the structural and morphology and *in situ* signals are considered.

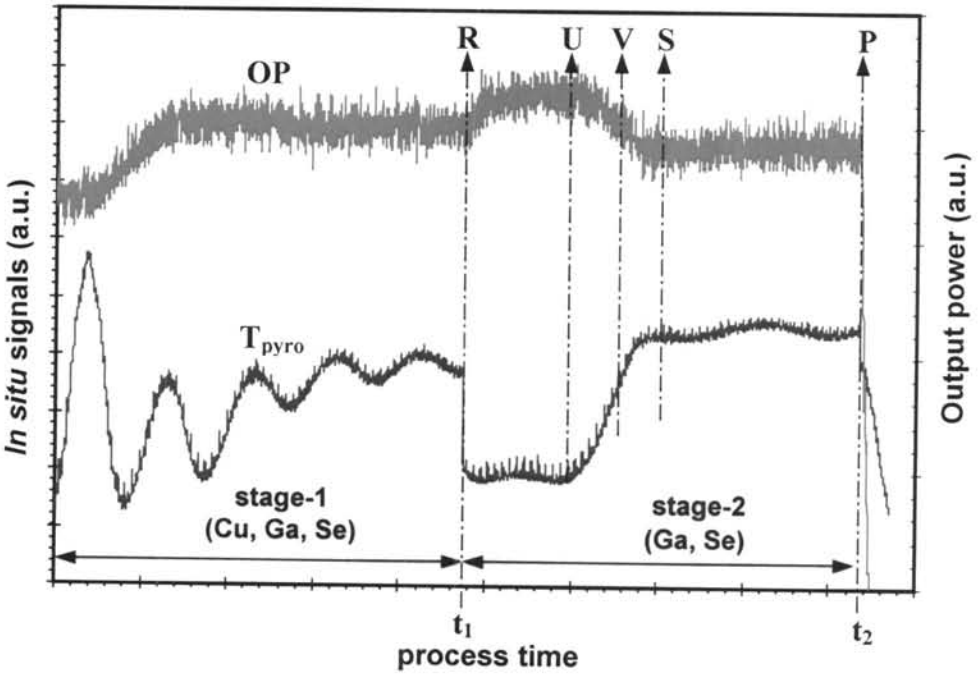

Figure 5.9: Profiles of *in situ* monitoring signals.

$CuGaSe_2$ films with Cu/Ga-ratio (y) of 1.45, 1.20, 1.10, 0.90, and 0.70 were grown by MBD on Mo-coated soda-lime glass substrates. Fig. 5.9 shows the typical profiles of *in situ* monitoring signals during the growth process. From the process parameters, $CuGaSe_2$ thin films of varied Cu/Ga-ratio from 1.45 to 0.70 can be obtained with high precision (as described in Section 5.1). The spiky signal which

superimpose the T_{pyro} signal is due to the radiation pass through the non Mo-coated area. Its small period corresponds to the rotation speed of the substrate. During stage-1, the oscillations of T_{pyro} correspond to the interference coming from the increase of the film thickness. In this stage, the calculated content of Cu/Ga-ratio is equal to 1.45 (point R). At the end of stage-1 (t_1), the Cu source is turned off and the film evolves to Cu-poor composition.

To investigate the structural and morphology evolution as well as the optical properties of films from Cu-rich to Cu-poor, the XRD, AFM, optical transmittance and optical reflectance measurements were carried out on the deposition-interrupted samples. The deposition of each samples was interrupted at point R (Cu-**R**ich: $y \approx 1.45$), point U ($y \approx 1.10$), point V ($y \approx 1.00$), point S (Cu-near **S**toicheometric: $y \approx 0.90$) and point P (Cu-**P**oor: $y \approx 0.70$) in Fig. 5.9. We named these samples as film **R**, film **U**, film **V**, film **S** and film **P**, respectively.

The different phases and the crystal structures of these films were determined by XRD using CuK_α radiation. The surface morphology of the films was examined using a combination of AFM and SEM. The thicknesses of films can be determined using the relation between refractive index as a function of wavelength and the optical interference fringes from reflectance spectra as described in the previous section. In this section, the thickness of the $CuGaSe_2$ films with various of Cu/Ga-ratios were measured directly from the cross-sectional SEM images of cleaved samples. The AFM was performed using a Digital Instruments Nanoscope III operating in non-contact tapping mode. The collected data consisted of height information on square 5x5 μm^2. The root-mean-square roughness (z_{rms}) were determined using section analysis.

The crystal parameters of some representative films: the film **R**, **S** and **P** were analyzed by XRD and shown in Fig. 5.10. As described above, these films were grown at the same set of temperatures of substrate and all elemental sources (Cu, Ga,

Se) but ended at different growing time. The film **R** represents the uniform Cu-rich film ended at Cu/Ga-ratio ≈ 1.45, the initial content of Cu used in the process. The film **S** and **P** were ended at Cu/Ga-ratio ≈ 0.90, 0.70 (extended Cu-poor), respectively. The preferred orientation along the (112) analyzed with respect to the (220)(204) peak intensity ratio, z = I(112)/I(220)(204), of these films is considered to be comparable to that of the standard powder from the bulk data file (JCPDS: 75-104). The lattice parameters a, c and c/a were also determined and shown in Table 5.4.

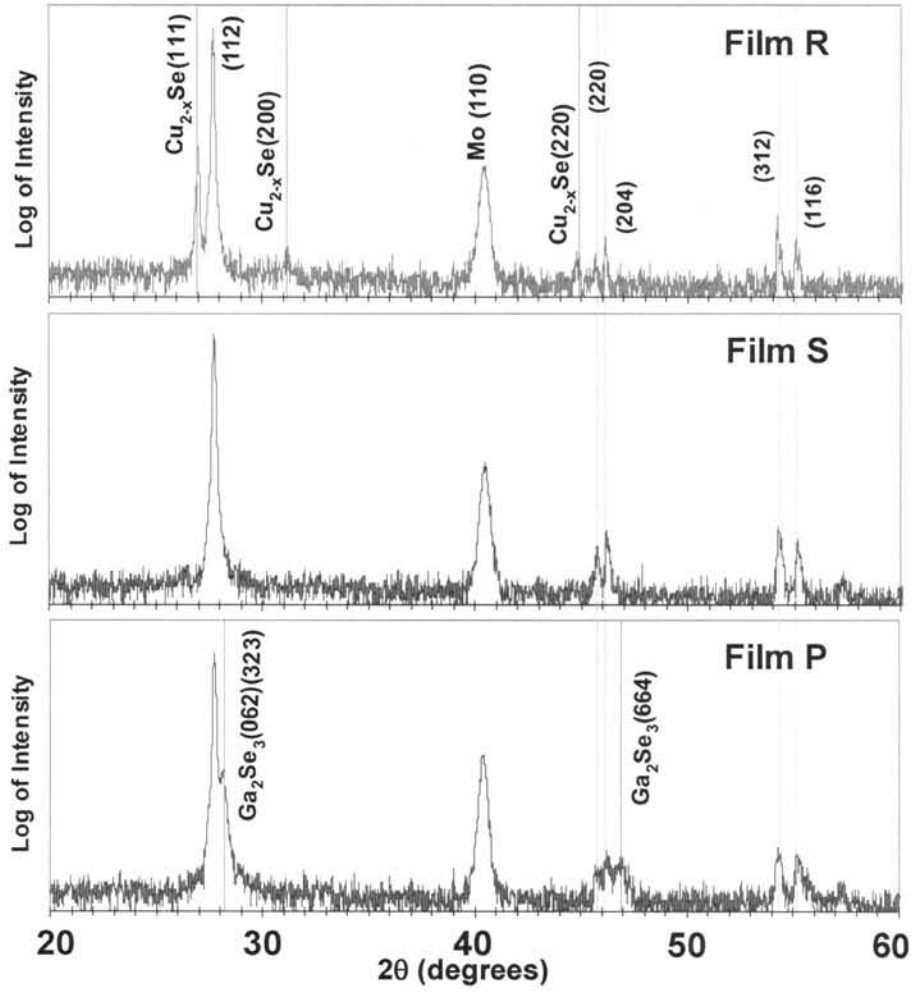

Figure 5.10: XRD spectra of the films **R**, **S** and **P** represent the evolution of $CuGaSe_2$ films grown by two-stage process as shown in Fig. 5.9.

Table 5.4: Calculated values of a, c, c/a and z from the XRD patterns of the films **R**, **S** and **P** shown in Fig. 5.10 and JCPDS of $CuGaSe_2$.

Sample	a (Å)	c (Å)	c/a	z	Qualified as:	Phase present
$CuGaSe_2$*	5.612	11.030	1.965	1.7	Random	
Film **R**	5.611	11.000	1.961	175.3	Textured (112)	$Cu_{2-x}Se + CuGaSe_2$
Film **S**	5.599	10.990	1.963	82.9	Textured (112)	$CuGaSe_2$
Film **P**	5.599	10.979	1.961	89.1	Textured (112)	$CuGaSe_2 + Ga_2Se_3$

* JCPDS: 75-104

The series of XRD spectra of the film **R** ($y \approx 1.45$), film **S** ($y \approx 0.90$) and film **P** ($y \approx 0.70$) shown in Fig. 5.10 indicated that they are polycrystalline films with strongly preferred (112) orientation. The full width at half maximum (FWHM) of these diffraction peaks is small indicating that the crystallinity is good. All of these films are in agreement with the diffraction lines in the chalcopyrite structure with or without the secondary phases $Cu_{2-x}Se$ and Ga_2Se_3 as described following. The XRD pattern of film **R** shows the mixed phases between a chalcopyrite phase $CuGaSe_2$ and a $Cu_{2-x}Se$ phase. All of the observed peak positions for the $Cu_{2-x}Se$ phase match the berzelianite (JCPDS: 6-680) with $x \approx 0.15$ which belongs to the cubic system with a=5.739 Å, due to reflections from (111), (200) and (220) planes of the reported structure. The presence of the additional phase $Cu_{2-x}Se$ in Cu-rich film is consistent with compositional measurements made using EDS as summarized in Table 5.5. However, this phase has not been found in both films **S** and **P**, which confirmed that this phase had been completely converted to single chalcopyrite phase.

Some research groups have reported that the structural properties of Ga-rich differed from those of Cu-rich films. Chichibu *et al.* [32] have revealed the appearance of the Ga-rich films contained extra phases such as β–Ga_2Se_3 and Cu_2Se. Yamada *et al.* [75] have shown that the XRD pattern of Ga-rich film, $y = 0.66$, lacks

the features of chalcopyrite structure and it is considered to have sphalerite crystalline structure. In contrary to their results, the Cu_2Se compound was not found in the XRD spectra of our $CuGaSe_2$ films with Ga-rich composition prepared by MBD. Moreover, the film **P** grown with extended decrease of Cu content and ended at Cu/Ga-ratio ≈ 0.70 shows lattice constant both a and c to be constant and no significant 2θ shift of the (112) peak was observed. This result implied that film **P** with chalcopyrite structure can tolerate an excess of several percent of Ga_2Se_3 over Cu_2Se without precipitation of extra diffraction peaks (i.e. (002), (110), (200)(004), (202) and (114)) caused by the ordering of vacancies in the defect-chalcopyrite structure.

Table 5.5: Summary of the chemical composition of representative $CuGaSe_2$ films presented in Fig 5.9.

Sample	Cu (at%)	Ga (at%)	Se (at%)	[Metal]/[Se]	y≡ [Cu]/([In]+[Ga])
Film **R**	32.23	19.39	48.38	1.07	1.45
Film **U**	26.82	24.46	48.72	1.05	1.10
Film **V**	26.07	26.04	47.89	1.09	1.00
Film **S**	25.41	25.13	49.46	1.02	0.90
Film **P**	16.81	33.73	49.46	1.02	0.70

The results of XRD spectra indicated that under Cu excess condition (stage-1), stoichiometric $CuGaSe_2$ was formed together with a second phase $Cu_{2-x}Se$ which segregated to the surface. During the Cu-off condition (stage-2), stoichiometric $CuGaSe_2$ was formed from the expense of $Cu_{2-x}Se$ and the Ga and Se flux (film **S** in Fig. 5.9). Consequently, the $CuGaSe_2$ compound ceased to grow after the second phase $Cu_{2-x}Se$ was consumed and a new second phase Ga_2Se_3 was segregated instead for the Cu-poor films. These XRD results revealed that the $CuGaSe_2$ films with

composition in the range of Cu/Ga from 1.45 to 0.70 show high crystalline tetragonal structure with strongly preferred (112) orientation without the indication of any distortion. FWHM of (112) diffraction peak for film **P** is larger than that of film **R**, this means that the crystallite size of the Cu-poor $CuGaSe_2$ film is smaller comparing to the Cu-rich film. The results of XRD spectra are consistent with the SEM and AFM studies on the surface morphology of $CuGaSe_2$ thin films as following.

For the SEM investigations, the cross-sectional and planar views of $CuGaSe_2$ films are shown in Fig. 5.11(a)-(e).

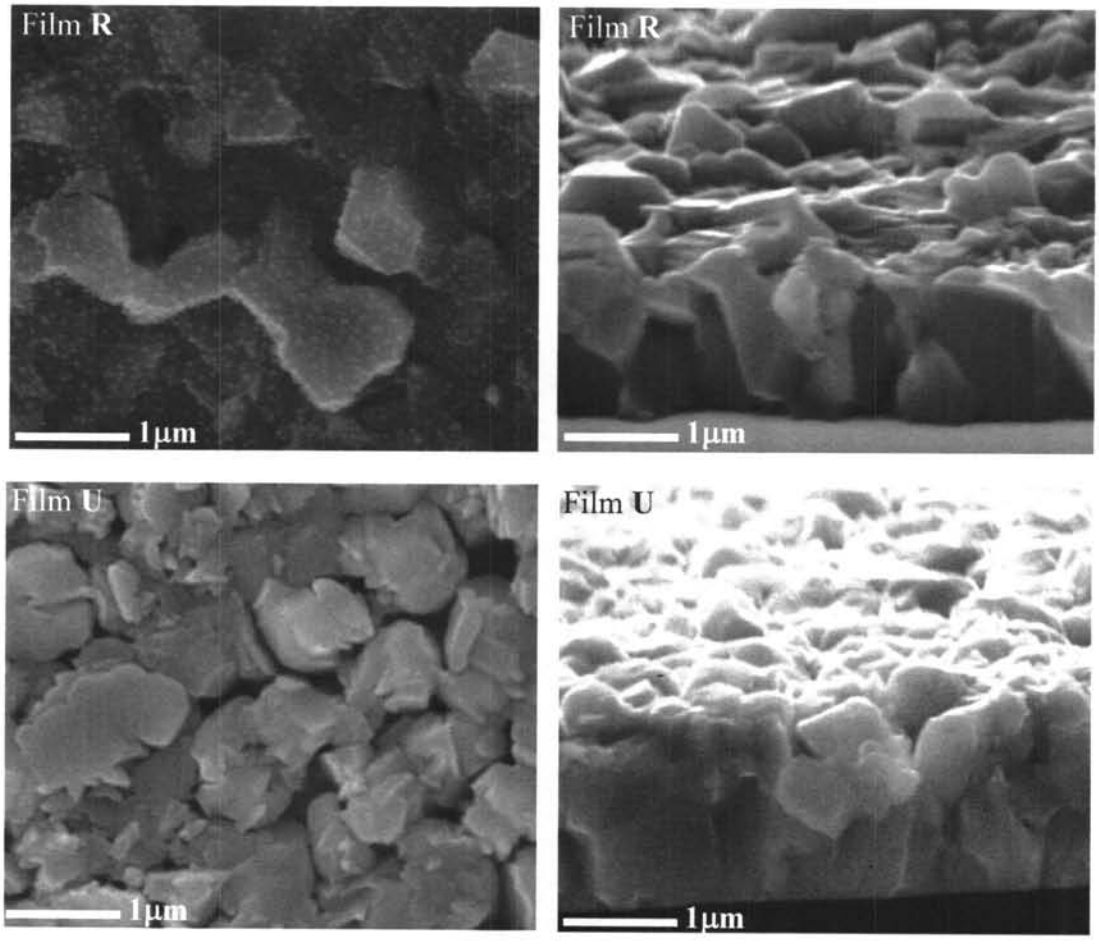

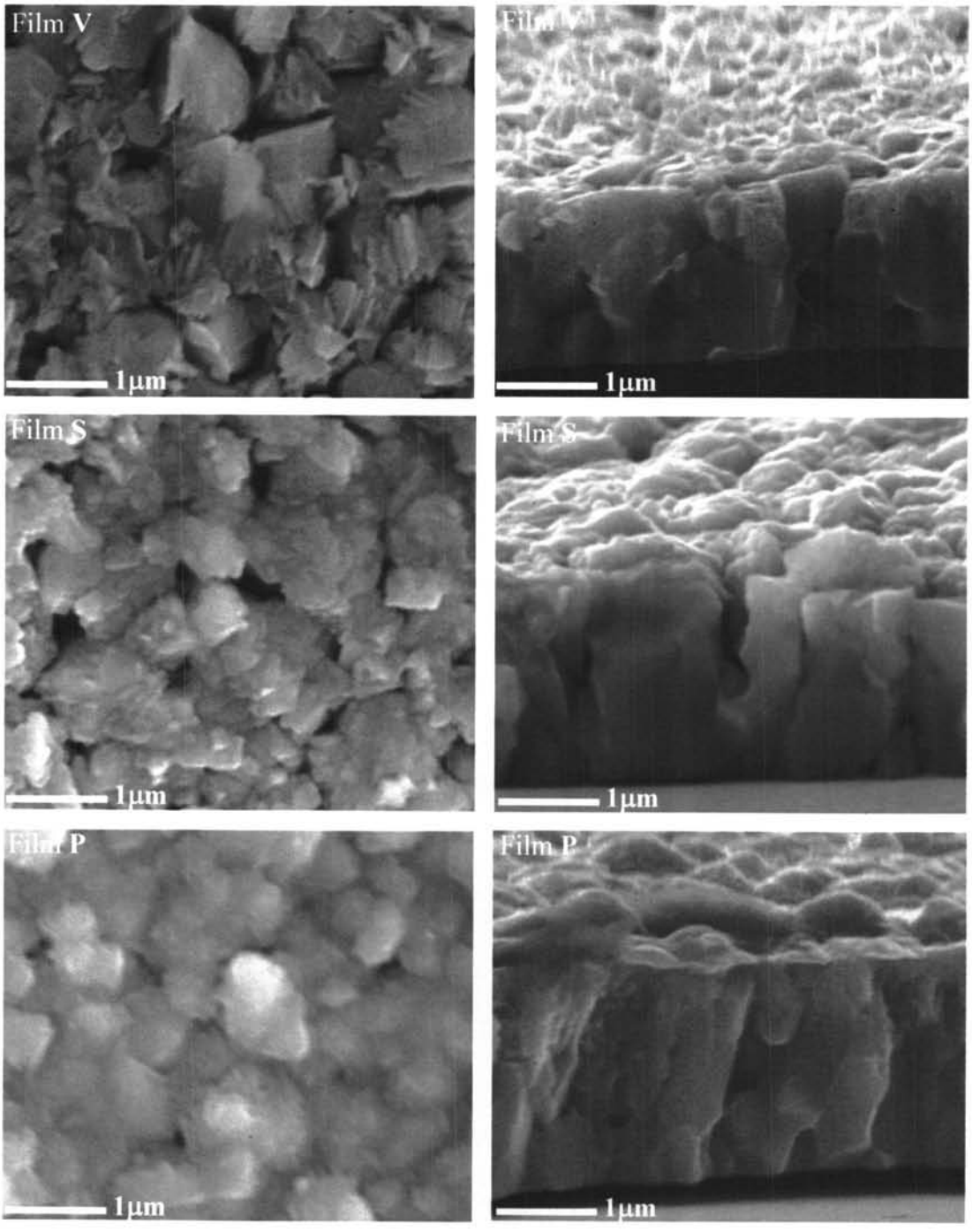

Figure 5.11: Surface and cross-section SEM images of $CuGaSe_2$ films with various Cu/Ga-ratios prepared by two-stage process.

Figure 5.11 shows the surface morphology and cross section of each film revealed by SEM at magnification of 10,000x. Film **R**, Fig 5.11(a) represents the uniform Cu-rich film with $y(t_1) \approx 1.45$ at the end of the 1st stage. The morphology of this film shows the densely columnar grain packing which contains the mixed phase systems; the $CuGaSe_2$ and $Cu_{2-x}Se$ as identified in the XRD results. During the 1st stage of growth process, these growing grains are expected to have the liquid phase of Cu_xSe compound at the surface of the growing film and between the grain boundaries. The binary phases segregate almost completely at the grain surfaces while the grain themselves are nearly stoichiometric of $CuGaSe_2$ with none or minor copper chalcogenide inclusions. The expectation of the existence of the liquid phase of Cu_xSe is confirmed by the followed films **U** and **V** with Cu/Ga-ratios equal to 1.10 and 1.00, respectively. Both of film **U** and **V** show the similar evidences of the revealed crevices between the $CuGaSe_2$ grain boundaries at the top fraction of the films as shown in the cleaved cross-section images. While the content of Cu decreases from the uniform Cu-rich with $y \approx 1.45$ to the nearly stoichiometric with $y \approx 1.00$, the formation of additional $CuGaSe_2$ chalcopyrite is expected to grow from the top fraction of the growing film by consuming Cu_xSe at the surface grains, whereas the bottom fraction of the films is still dense without void. The initial appearance of their crevices between the $CuGaSe_2$ grain boundaries can be hypothesized to be the out diffusion of the liquid phase of Cu_xSe into the binary phase of Ga_2Se_3 from the incoming fluxes of Ga and Se at surface. The important influence of the liquid Cu_xSe phase on the growth of Cu-rich film is to induce large, nearly stoichiometric chalcopyrite grains with high structural perfection and good electronic properties [76]. The presence of Cu_xSe on the surface acts as "flux" with a high diffusion coefficient for atomic species involved in the growth process. To date, there does not exist any direct evidence of a liquid Cu_xSe phase during the growth or of a solid CuSe phase upon cooling in the Cu-rich film [77, 78].

As previously described, it is important to understand the completed conversion from the secondary phase towards the end of the growth process without affecting the good properties of already grown chalcopyrite film. Film **S** with Cu/Ga-ratio ≈ 0.90 and the extended Cu-poor (film **P**) with y ≈ 0.70 continued to grow with the same fluxes of Ga and Se in stage-2. The morphology and cross-section of film **S** (see Fig. 5.11 (d)) exhibit the surface grains and columnar grains rounder and slightly larger, respectively, than that of film **U** and **V**. Especially, the deep crevices of film **S** are clearly observed. Film **P** exhibits the different surface with small grains of the excess Ga_2Se_3 compound and the disappearance of their deep crevices by filling the Ga_2Se_3 compound without re-crystallization into their $CuGaSe_2$ grains. The behaviors of the excess Ga_2Se_3 compound can be explained in a straightforward manner only if the stabilized $CuGaSe_2$ phase without Cu migration is assumed. All above aspects would be expected to agree with the disappearance of the binary phase of $Cu_{2-x}Se$ from the Cu-rich film to the nearly stoichiometric at EPD, and the appearance of the excess of Ga_2Se_3 compound in the extended Cu-poor film as identified in the XRD result.

The morphological features of these films as shown in Fig 5.12, Cu-rich film (film **R**) show large facetted-grain size and high roughness with a root-mean-square surface roughness (z_{rms}) of 126.7 nm. The appearance of the large facetted grains is due to the presence of copper selenide corresponding to the $Cu_{2-x}Se$ diffraction signals in XRD spectra of film **R** in Fig. 5.10. Film **S**, nearly stoichiometric composition also shows large grain size, surface roughness of 98.5 nm with deep crevices between grain boundaries because the $Cu_{2-x}Se$ is completely consumed. Consequently, the new second phase Ga_2Se_3 was formed from the excess Ga and Se flux covering the surface. Thus the morphology of film **P** with surface roughness of 87 nm is relatively smooth in comparison with those of film **R** and film **S** as shown in AFM picture of film **P**.

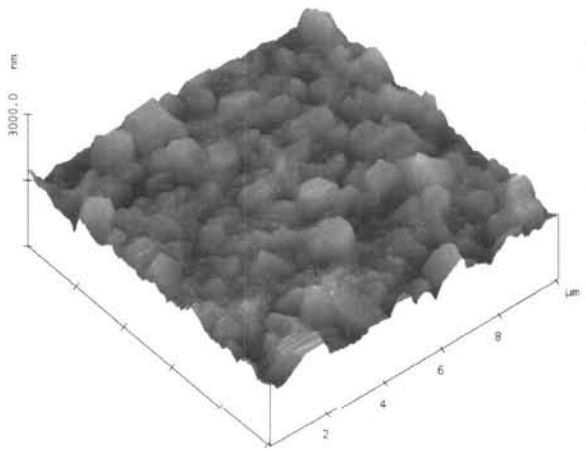

Film **R**: $CuGaSe_2 + Cu_{2-x}Se$

Large grains, sharp, rough surface

$z_{rms} = 126.7$ nm

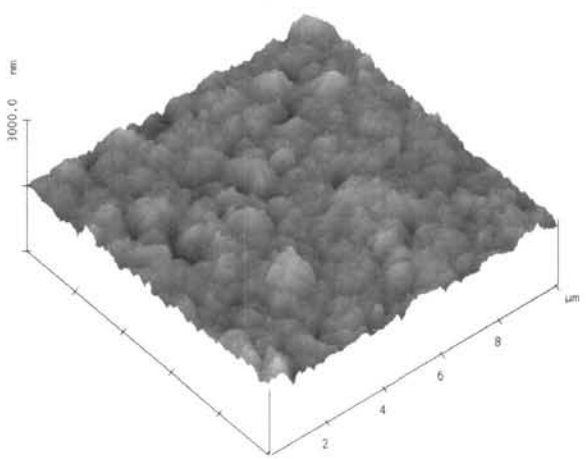

Film **S**: $CuGaSe_2$

Large grains, deep crevices between grain boundaries at the top of surface

$z_{rms} = 98.5$ nm

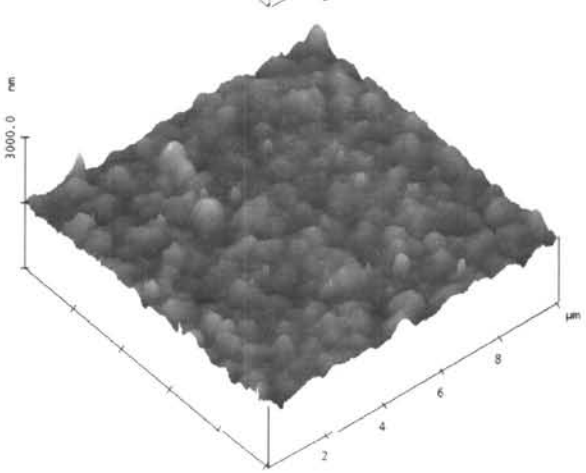

Film **P**: $CuGaSe_2$

Small grains, smooth surface

$z_{rms} = 87.0$ nm

Figure 5.12: AFM pictures of selective $CuGaSe_2$ thin films: film **R** (Cu/Ga ≈ 1.45), film **S** (Cu/Ga ≈ 0.90) and film **P** (Cu/Ga ≈ 0.70).

Figure 5.13 shows the optical absorption spectra at room temperature of the $CuGaSe_2$ polycrystalline thin films plotted as a function of Cu/Ga-ratio in the photon energy range of 1.50 to 2.00 eV. The optical properties of all $CuGaSe_2$ films prepared by MBD are consistent with the XRD analysis as following. The XRD patterns of all MBD $CuGaSe_2$ films showed a predominant (112) orientation with very weak intensities from other diffraction peaks (except Mo (110) peak), indicating that the films contain less numbers of grain boundaries as well as lattice defects. Therefore, all $CuGaSe_2$ films exhibits a clear free exciton (FE) absorption peak even at room temperature as described in section 5.1.

The examples of the results of the fitting optical absorption spectra of Cu-rich $CuGaSe_2$ thin film (film **R**) including exciton absorption are shown in Fig. 5.14.

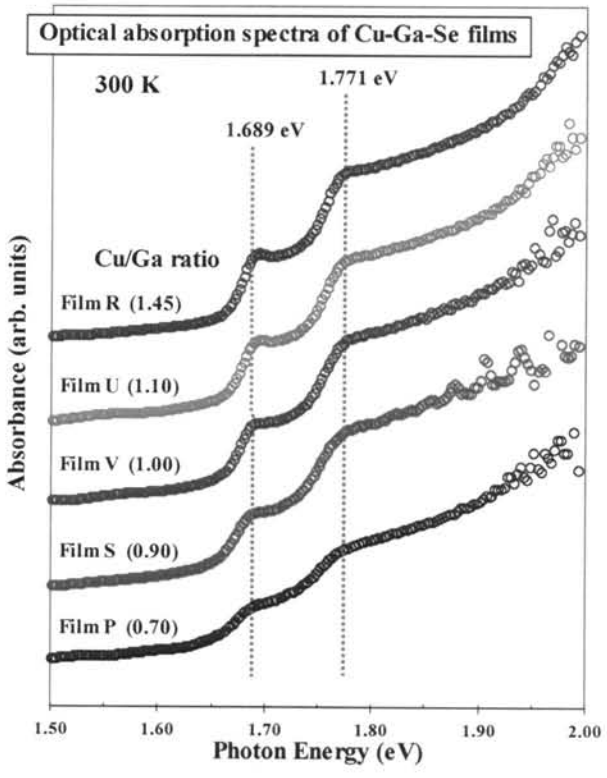

Figure 5.13: Optical absorption spectra of $CuGaSe_2$ thin films with Cu/Ga-ratio ranging from 1.45 to 0.70 measured at room temperature.

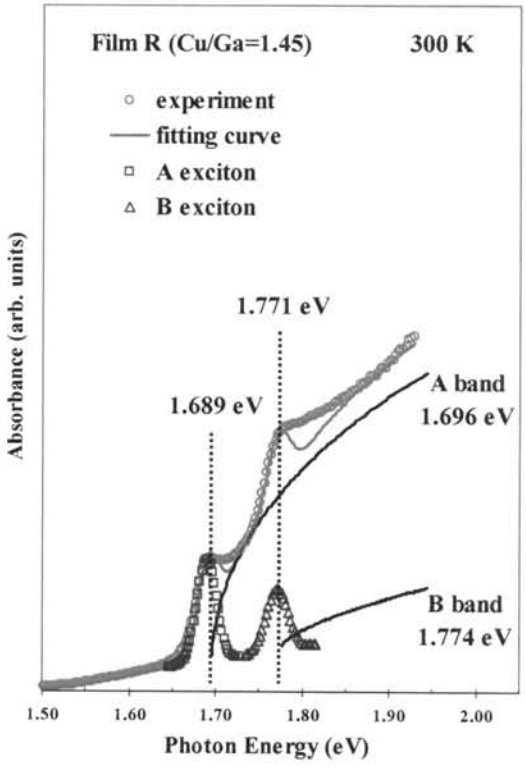

Figure 5.14: Typical result of the simplified fitting method for the optical absorption spectrum of $CuGaSe_2$ thin film (film **R**).

The summation of the fitting curves (solid line) nearly coincide with the experimental measurement data (open-circle line). This simplified fitting method can be used for the $CuGaSe_2$ thin films from Cu-rich to Cu-poor compositions. Two free excitonic resonance energies (1.689 and 1.771 eV) and two direct allowed transition energy, A and B, (1.696 and 1.774 eV) were determined from the fitting for all $CuGaSe_2$ thin films. Both E_g and free excitonic resonance energy of the films were found to be no significantly change with Cu/Ga-ratios from 1.45 to 0.70. The amount of free exciton was slightly decreased with decreasing of Cu/Ga-ratio. This effect was expected to be due to a secondary phase (Ga_2Se_3) formed from Ga-excess on the extended Cu-poor film (film **P**). The contribution of excitonic absorption in optical absorption spectra observed in wide range of Cu/Ga-ratio implied that the crystallographic structure of all films is good.

5.3 Growth and Characterization of $CuGaSe_2$ Thin Films Grown by MBD Using Three-stage Process

5.3.1 *in situ* Monitoring Signals of the Growth of $CuGaSe_2$ Thin Films Using Three-stage Process

As previously discussed in Section 4.2.3 about the growth of $CuGaSe_2$ thin films by the MBD method using the three-stage process, the typical temperature profiles (deposition rates) of three elemental sources (Cu, Ga and Se) and substrate temperature (T_{sub}) are shown in Fig 5.15. In our standard process, the substrate temperature during the first stage was 340°C and the maximum temperature in 2nd and 3rd stage was 520°C. The time interval of about 10 minutes was consumed during raising the substrate temperature up. The temperatures of all the sources were chosen for total film thickness of approximately 2 μm and for total deposition time of 150 minutes.

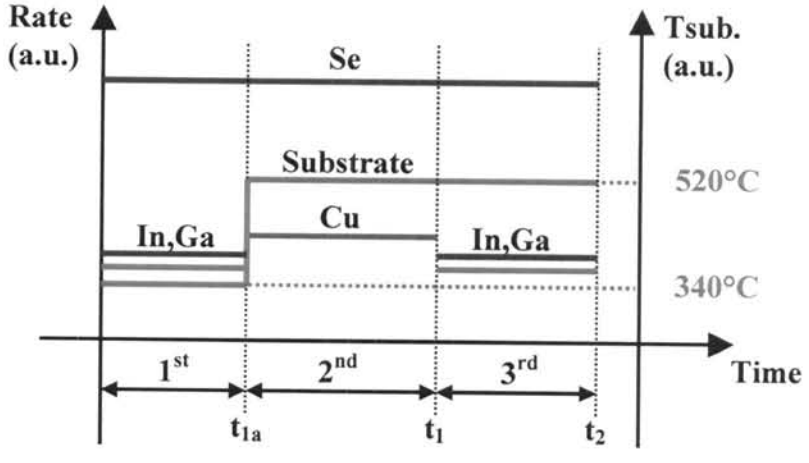

Figure 5.15: Typical temperature profiles of Cu, Ga and Se sources and the substrate temperature (T_{sub}) in the three-stage process of $CuGaSe_2$ thin film growth.

During the growth process as shown in Fig. 5.16, the *in situ* monitoring signals were also employed to study the evolution of the growing film, to indicate a critical amount of Cu-rich composition at t_1 in the end of the 2nd stage, and to detect a desired Cu-deficient composition ($y \approx 0.90$) at t_2. These signals show typical variations of the sample surface temperature, as detected by the pyrometer (T_{pyro}), the output power (OP) of the temperature controller which keeps the substrate temperature by tracing the profile of substrate itself.

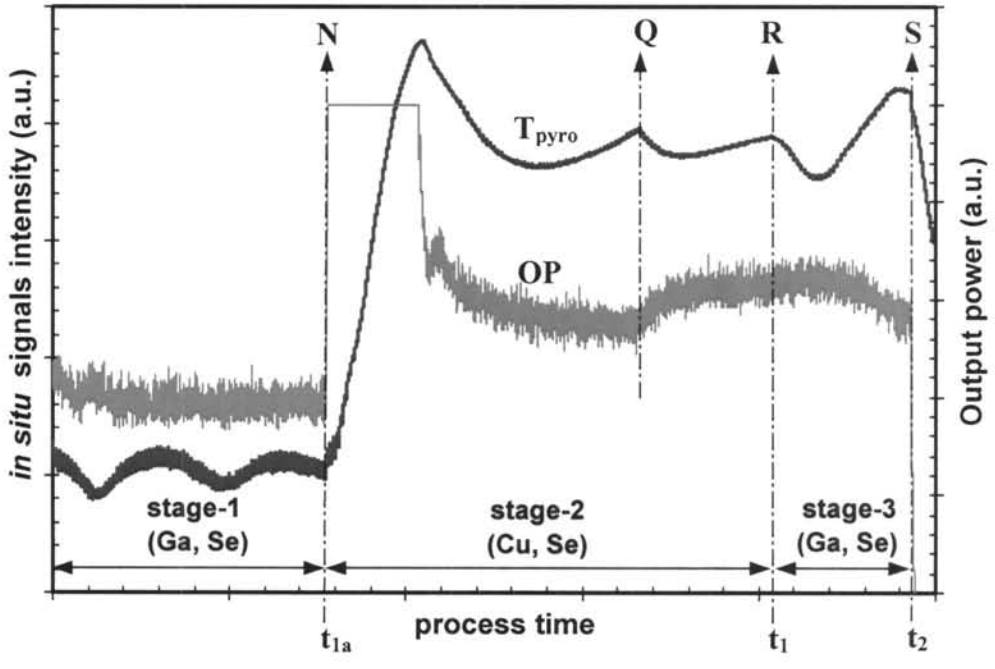

Figure 5.16: Typical profiles of the *in situ* monitoring signals; T_{pyro} and OP during the three-stage process of $CuGaSe_2$ films.

During the 1st stage (after the shutter is opened at t=0), the Ga_2Se_3 precursor starts to grow by incoming fluxes of Ga and Se at low temperature. The OP signal slightly decreases to a certain minimum value, whereas the T_{pyro} signal exhibits the oscillation which is the result of the optical interference by thin film as detected at the 1.55 μm radiation. During the 2nd stage, when the substrate temperature rapidly rises to the maximum temperature, the OP of the controller must be increased to a maximum value for a short period until the T_{sub} reaches 520°C. Then the OP signal

decreases to a certain value as long as the film is Cu-poor composition. At the same period, the T_{pyro} signal shows the different oscillation which is the result of adding Cu-Se onto Ga_2Se_3 precursor. We expect that the incoming atoms of Cu and Se diffuse into the Ga_2Se_3 precursor. Especially, Cu can diffuse homogeneously throughout the $Cu(In,Ga)Se_2$ film with an (In,Ga)-rich composition as previously report [79].

A long period of the oscillation is observed in the T_{pyro} signal. We note that the oscillation is caused by the different refractive index of the $CuGaSe_2$ growing film with various Cu contents in a Cu-poor region. During the growing film continuously increases the Cu content to cross a stochiometric to Cu-rich region, both signals show the two coherent changes. The T_{pyro} signal shows a reversed oscillation with a similar period, whereas the OP signal increases to a certain equilibrium value. We would like to point out that the abrupt changes is caused by the sufficient chalcopyrite phase in the growing film and the different morphology with high emissivity. We also attribute these abrupt changes to the point indicating that the $CuGaSe_2$ film has been transformed to the stoichiometric film. The composition of the $CuGaSe_2$ film which is ended at this point (point Q) has been analyzed by the EDS technique to be $y \approx 1.00$. The process time at the point Q is named as t_{stoi}. After the point Q, the Cu-rich film starts to grow with the excess fluxes of Cu and Se. We expect that the Cu_xSe phase exists on the surface film and between the $CuGaSe_2$ grain boundaries as proposed in [80, 81].

At the 3rd stage when the Cu flux is changed to Ga flux, the growth of the $CuGaSe_2$ film is formed by Ga, Se fluxes and Cu from the segregated Cu_xSe phase. On the expense of the Cu_xSe phase in the Cu-rich $CuGaSe_2$ film, the emissivity of the growing film can be expected to decrease during the growing film continuously decreases the Cu content to cross a stoichiometric to Cu-poor region. Both signals show the similar transition signals which can be used to indicate the desired Cu-

deficient composition at EPD in the three-stage process. Moreover, in order to understand the three-stage growth process, a set of four samples consists of the films N, Q, R and S (as indicated in Fig. 5.16) were grown at the same set of temperature profiles but interrupted at different growing time.

5.3.2 Evolution of Crystal Structure of the $CuGaSe_2$ Films Grown by Three-stage Process

Figure 5.17 shows the typical X-ray diffraction patterns of the films N, Q, R and S that represent the evolution of the film grown during the three-stage process as indicated in Fig. 5.16. The film N represents the Ga_2Se_3 precursor interrupted at $t_{1a} \approx$ 47 min without Cu content (y=0). The film Q, R and S were interrupted at $t = t_{stoi} \approx$ 102 min, $t = t_1 \approx 125$ and $t = t_2 \approx 150$ min, respectively. The film Q is the result of a sufficient chalcopyrite phase at t_{stoi} was indicated by the abrupt change of the monitoring signals. The film R is the result of a Cu-rich film with $y \approx 1.30$ as analyzed by the EDS technique. The film S is the result of a completed three-stage process at EPD with $y \approx 0.90$ (desired Cu-deficient). The chemical composition of these films was analyzed by the EDS technique and the ratios of these values were also determined and shown in Table 5.6.

Table 5.6: Summary of the chemical composition of representative $CuGaSe_2$ films presented in Fig. 5.16.

Sample	Cu (at%)	Ga (at%)	Se (at%)	[Metal]/[Se]	[Cu]/([In]+[Ga])
Film **N**	0.00	38.27	61.73	0.62	0.00
Film **Q**	24.86	24.38	50.76	0.97	1.02
Film **R**	28.58	22.16	49.26	1.03	1.29
Film **S**	23.06	25.92	51.02	0.96	0.89

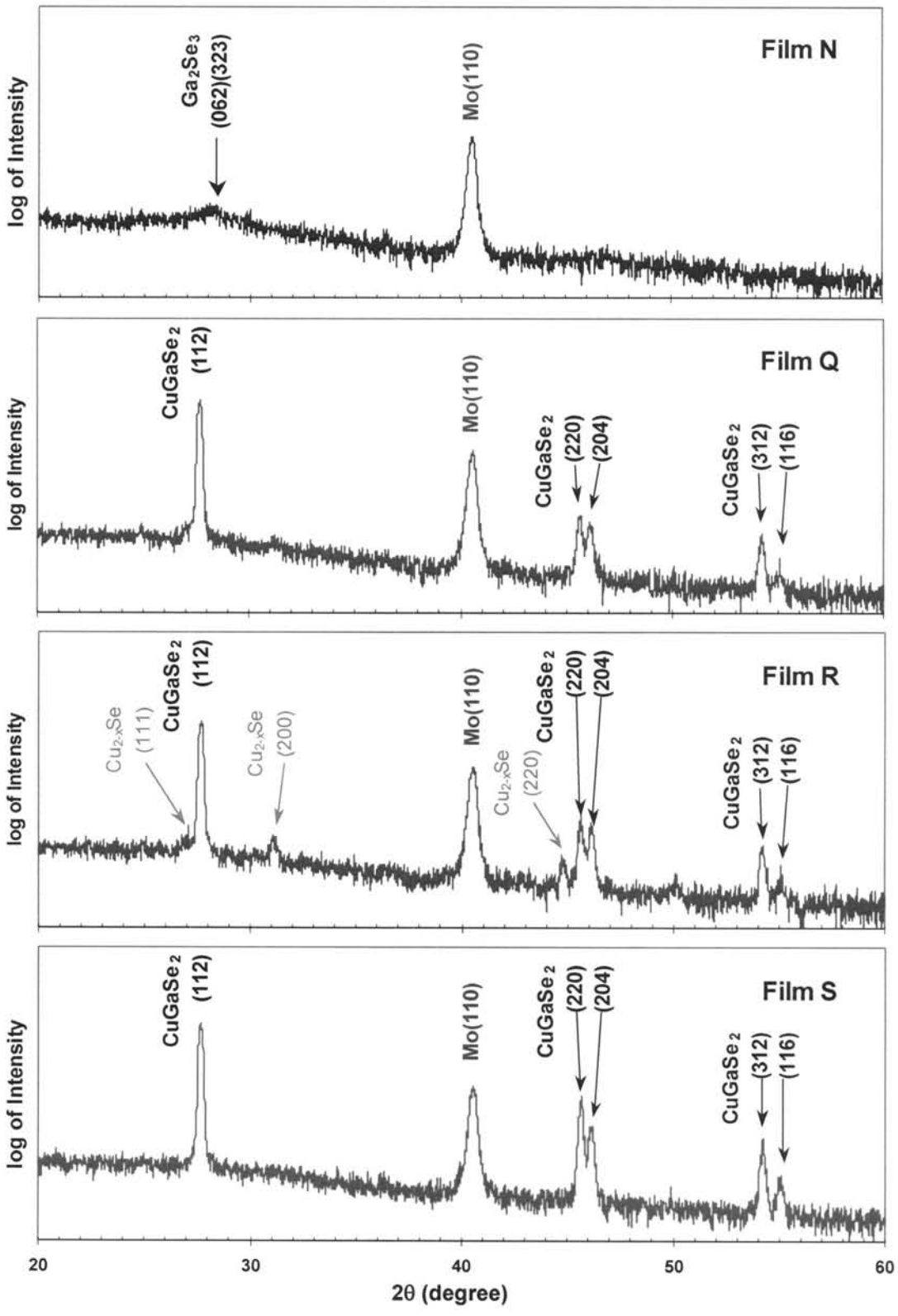

Figure 5.17: XRD spectra of the films N, Q, R and S represent the evolution of $CuGaSe_2$ films grown by three-stage process as shown in Fig. 5.16.

The typical XRD pattern of film N shows a low crystallinity or amorphous of Ga_2Se_3 precursor coated on Mo/SLG substrate, where the diffraction peak of Mo polycrystalline film coated on the SLG substrate is clearly observed to be the preferred (110) orientation parallel to the SLG substrate. The typical XRD spectra of films Q, R and S show well-defined peaks suggesting that the samples have almost perfect polycrystalline films. The standard JCPDS (Joint Committee on Powder Diffraction Standards) cards were used to analyze the structural properties of these films. All of the peaks are in agreement with the standard diffraction lines in the chalcopyrite structure. The XRD spectra of film Q and S are observed to be a α-phase of $CuGaSe_2$ structure, whereas the XRD pattern of film R consists of the mixed phase between a chalcopyrite $CuGaSe_2$ and $Cu_{2-x}Se$ phase match the berzelianite (JCPDS: 6-680), with $x \approx 0.15$ which belong to the cubic system with lattice constant a= 5.739 Å, due to reflections from (111), (200) and (220) planes of the reported structure [81]. The presence of the small additional phase $Cu_{2-x}Se$ in Cu-rich film is consistent with compositional analysis by EDS technique as shown in Table 5.6. The evolution of an orientation ratio, z = I(112)/I(220)(204), of the films Q, R and S is considered to be comparable to that of the standard powder from bulk JCPDS: 75-104. The lattice parameters a, c and c/a were also determined and shown in Table 5.7. The z ratios of the films Q, R and S revealed that the $CuGaSe_2$ films grown by three stage process show weakly (112) preferred orientation with chalcopyrite structure and no indication of any distortion. In comparison of films Q and S reveals that the peak splitting of the (220)(204) and the (312)(116) planes shown higher crystalline quality with smaller values of FWHM. This means that the crystallize size of the nearly-stoichiometric films at EPD (film S) is larger comparing to the film Q.

The XRD results of the films N, Q, R, and S grown by three-stage process demonstrated that the amorphous-Ga_2Se_3 precursor in film N was re-crystallized to be the chalcopyrite-type on the basis of $CuGaSe_2$ in film Q. A small amount of liquid-

Cu_xSe was then formed from the excess fluxes of Cu and Se. The liquid-Cu_xSe was segregated to the surface of $CuGaSe_2$ layer in film R. But the excess of Cu_xSe is difficult to identify by XRD at room temperature. As described above, Cu atom is distributed homogeneously in a $CuGaSe_2$ film with a Cu-poor composition. During the Cu-off condition in stage-3, a nearly stoichiometric film was formed form the completed expense of Cu_2Se by the incoming fluxes of Ga and Se. Therefore, the phases in the $CuGaSe_2$ films change along the Cu_2Se-Ga_2Se_3 pseudo-binary system as previously illustrated in Fig. 2.3. Furthermore, in order to understand the evolution of morphology and grain growth of the $CuGaSe_2$ films using three-stage process, the samples also were characterized using SEM and AFM. The images both surface and cross-section are shown in Fig. 5.18.

Table 5.7: Calculated values of a, c, c/a and z from the XRD patterns of the films N, Q, R and S shown in Fig. 5.17 and JCPDS of $CuGaSe_2$.

Sample	a (Å)	c (Å)	c/a	z	Qualified as	Phase present
$CuGaSe_2$*	5.612	11.030	1.965	1.7	Random	
Film **N**	-	-	-	-	Amorphous	Ga_2Se_3 precursor
Film **Q**	5.613	11.012	1.962	4.6	Weak (112)	$CuGaSe_2$
Film **R**	5.613	11.011	1.962	3.2	Weak (112)	$CuGaSe_2$ + $Cu_{2-x}Se$
Film **S**	5.612	11.014	1.963	2.2	Weak (112)	$CuGaSe_2$

*JCPDS: 75-104

5.3.3 Morphology and Grain Growth of the $CuGaSe_2$ Films Grown by Three-stage Process

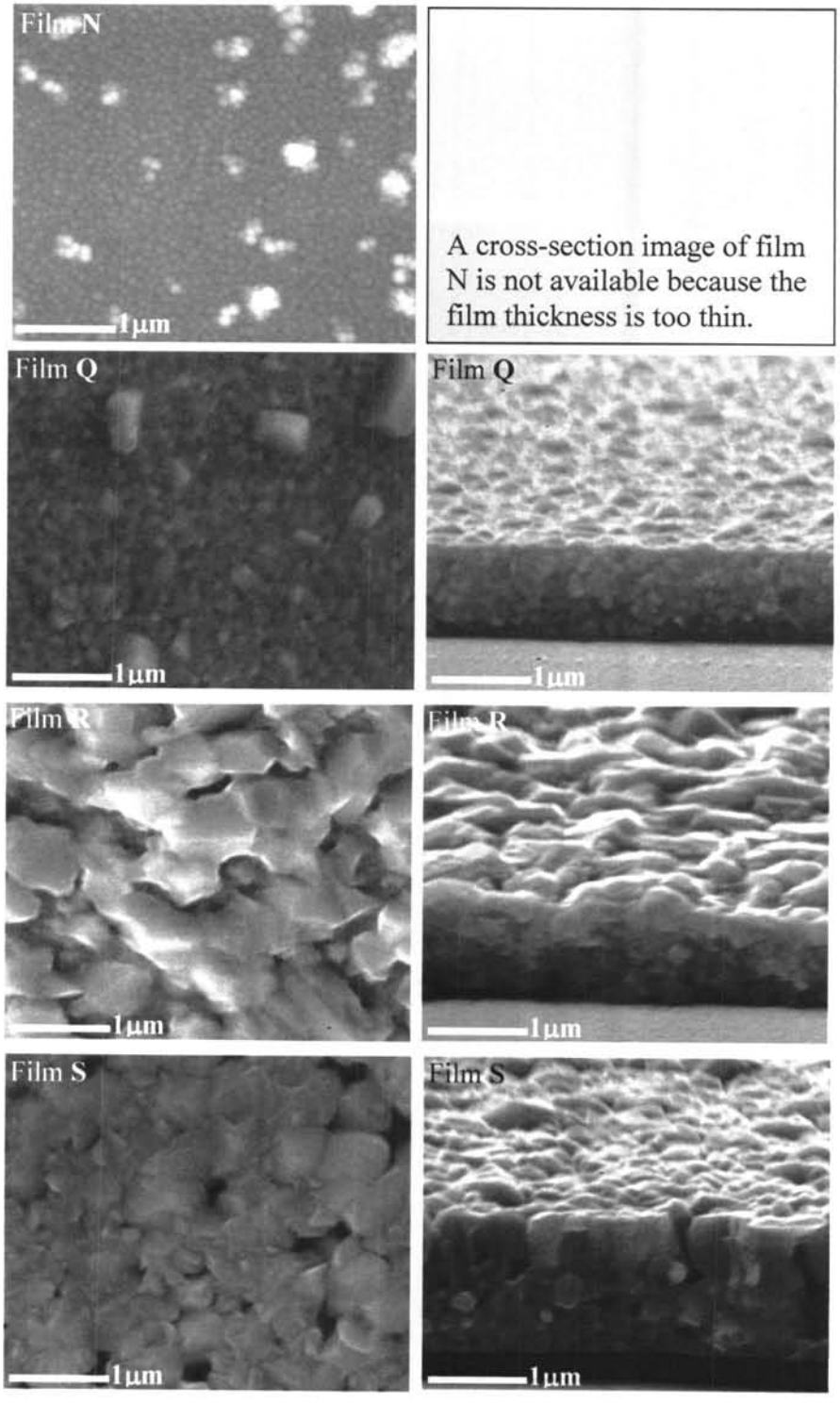

Figure 5.18: Surface and cross-section images of the films N, Q, R and S represent the evolution of film growth during the three-stage process as shown in Fig. 5.16.

Figure 5.18 shows the typical surface morphology and cross-section of the films obtained from the growth profile shown in Fig. 5.16. All SEM images were carried out at a magnification of 10,000x. Film N represents the uniform film of Ga_2Se_3 precursor at the end of the 1st stage. The morphology of film N shows smooth surface, small and dense grain packing with an average grain size of about 80 nm. These small grains represent the low crystalline quality as identified by the XRD results.

During the 2nd stage, the film Q is ended at almost stoichiometric composition (t_{stoi}) as indicated by the abrupt change of the monitoring signals. The morphology of film Q shows slightly rougher surface than that of film N. The crystallite sizes of film Q consists of majority medium sized grains of about 140 nm and some minority large sized grains between 0.2 to 0.5 μm at the surface of the film. The above observation is consistent with the evolution of their crystallinities from amorphous Ga_2Se_3 to almost stoichiometric $CuGaSe_2$ with chalcopyrite structure as illustrated in the XRD results. The film R with $y \approx 1.3$ is interrupted at the end of the 2nd stage (t_1). The morphology of film R shows a homogeneous covering of larger sized grains between 0.5 to 1.0 μm over the original crystallites at the bottom fraction of the film. We expect that the larger sized grains at the upper part of film R is the $Cu_{2-x}Se$ secondary phase as presented in the XRD results and also in the chemical composition analysis by EDS.

Finally, the film S at EPD with desired Cu-deficient composition ($y \approx 0.9$) as detected by the monitoring signals is ended at the end of the 3rd stage (t_2). The surface morphology of film S reveals the large sized grains between 0.5 to 0.8 μm which start on the top of the original crystallites (film Q). We expect that the formation of additional $CuGaSe_2$ chalcopyrite at the top fraction with large columnar grains is caused by the consuming of the liquid phase of Cu_xSe on the surface of the original crystallites. The deep crevices also are observed from the top fraction and limited by the medium sized grains of the original crystallites at the bottom traction which is still

dense without void. The origin of their crevices between the $CuGaSe_2$ grain boundaries also can be hypothesized to be the out diffusion of the liquid phase of Cu_xSe into the binary phase of Ga_2Se_3 from the incoming fluxes of Ga and Se at surface. The above results are consistent with the stability of the original $CuGaSe_2$ crystallites which not only can tolerate an excess of several percent of Cu_2Se during the growth of Cu-rich composition but also can maintain the stoichiometric $CuGaSe_2$ crystallites with chalcopyrite structure. Therefore, the three-stage process using the *in situ* monitoring signals as a control process would be expected to fabricate the higher quality $CuGaSe_2$ films with suitable properties for wide band gap absorber.

5.4 Solar Cell Devices Analysis

Using the end point detection as mentioned in Section 5.1.1, to control our $CuIn_{1-x}Ga_xSe_2$ growth process, $CuIn_{1-x}Ga_xSe_2$ films were prepared and the $CuIn_{1-x}Ga_xSe_2$ thin film solar cells with device structure Ni(Al)/ZnO(Al)/i-ZnO/CdS/$CuIn_{1-x}Ga_xSe_2$/Mo/SLG were fabricated as outlined in Section 4.1. In brief, the absorber films were coated with a 50 nm thick CdS buffer layer as soon as possible after absorber growth process. The CdS layer was then covered with a 50 nm highly resistive intrinsic ZnO layer, followed by a highly doped n-type ZnO film with typical thickness about 500 nm. The 50 nm Ni/1 μm Al front contacts were deposited onto the ZnO layers. The perimeters of individual cells were mechanically scribed to yield device areas of approximately 0.5 cm^2. The photovoltaic parameters such as conversion efficiency (η), fill factor (FF), open-circuit voltage (V_{OC}) and short-circuit current density (J_{SC}) were determined from J-V measurement carried out under condition with simulated AM1.5 (100mW/cm^2) at 25°C.

5.4.1 $CuIn_{1-x}Ga_xSe_2$ –Based Thin Film Solar Cells: Absorber Grown by Two-stage Growth Process

The influence of [Ga]/([In]+[Ga])-ratios of $CuIn_{1-x}Ga_xSe_2$ absorber layer grown by two-stage process on solar cell performances was also investigated with a similar set of samples as presented in Table 5.8. Each sample consisted of 8-10 uniform cells.

Table 5.8: The average values of photovoltaic parameters of $CuIn_{1-x}Ga_xSe_2$ thin film solar cells with various x of absorber layers grown by two-stage process.

[Ga]/([In]+[Ga]) ratio	V_{OC} (mV)	J_{SC} (mA/cm^2)	FF (%)	η (%)	R_S (Ω cm^2)
0.0	485 ± 5	32.4 ± 2.1	63.7 ± 0.4	10.0 ± 0.6	2.5 ± 0.3
0.3	600	25.3 ± 1.4	68.0 ± 1.2	10.3 ± 0.8	2.8 ± 0.4
0.5	636 ± 5	25.9 ± 1.8	64.2 ± 2.0	10.5 ± 0.5	3.5 ± 0.1
0.7	643 ± 7	24.9 ± 2.5	65.0 ± 0.5	9.8 ± 0.6	3.8 ± 0.3
1.0	620 ± 3	7.3 ± 0.6	57.9 ± 0.1	2.6 ± 0.2	12.6 ± 1.5

Figure 5.19 displays the photovoltaic parameters of the Ni(Al)/ZnO/i-ZnO/CdS/$CuIn_{1-x}Ga_xSe_2$/Mo/SLG solar cells under AM1.5 conditions. The absorber layers were grown by MBD using two-stage growth process. The cell performance of $CuIn_{1-x}Ga_xSe_2$ ($x \leq 0.7$) revealed that the V_{OC} values varied between 485 mV and 643 mV depending on the Ga content. J_{SC} varied between 24.9 and 32.4 mA/cm^2, while the fill factor values were limited to between 63.7 and 68%. These relatively low V_{OC} and J_{SC} as well as FF were attributed to limit the conversion efficiencies of our representative devices to around 10%. It is known that the replacement of the $CuInSe_2$ absorber film with a $CuIn_{1-x}Ga_xSe_2$ film yielded improvements in conversion efficiencies. In this research, however, the V_{OC} was below the estimated values. These

low V_{OC} indicated that the incorporation of Ga into $CuInSe_2$ absorbers only result in increasing of the band gap, E_g.

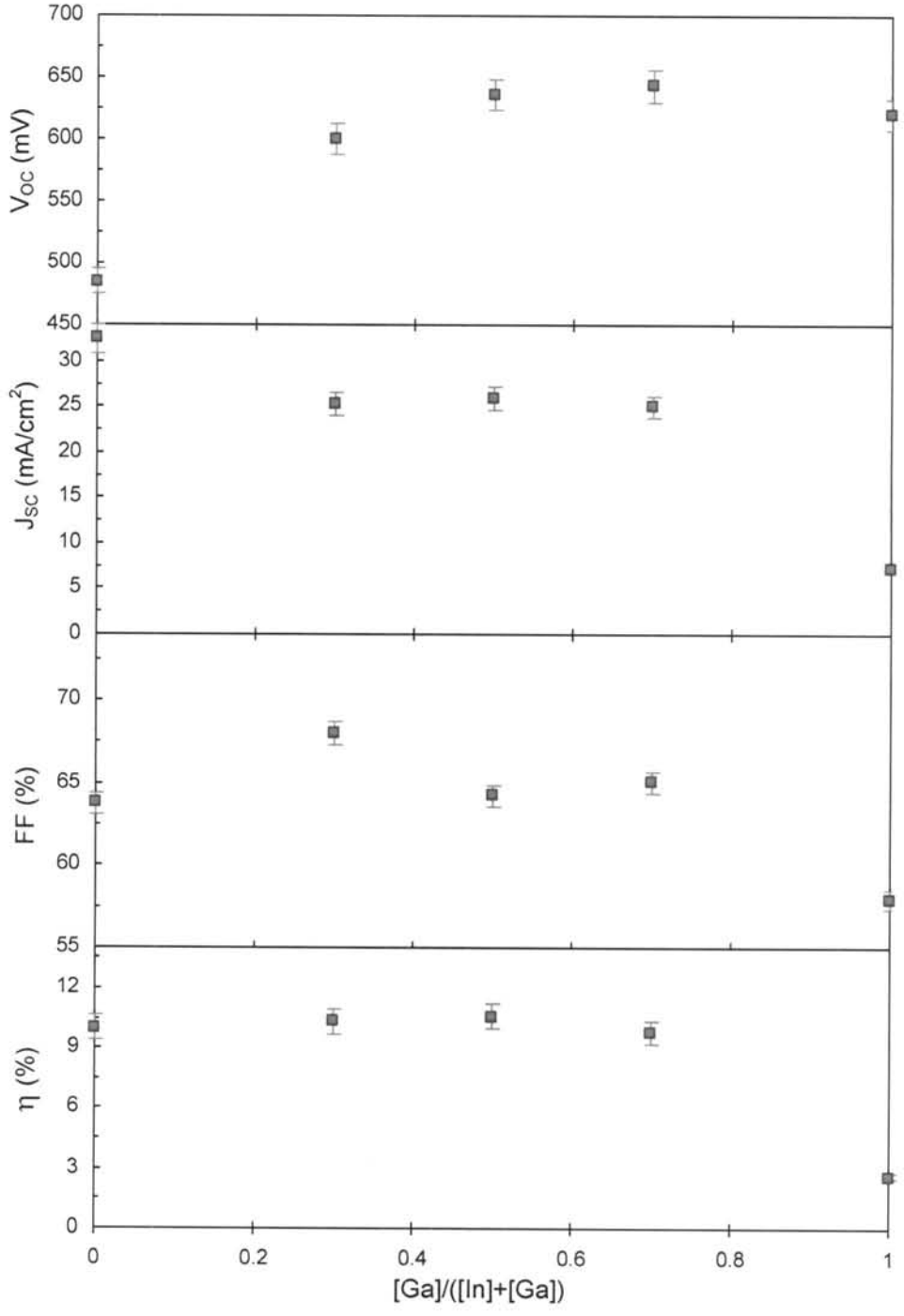

Figure 5.19: Average photovoltaic parameters of the Ni(Al)/ZnO/i-ZnO/CdS/ $CuIn_{1-x}Ga_xSe_2$/Mo/SLG solar cells with respect to the [Ga]/([In]+[Ga]) ratio based on as-grown $CuIn_{1-x}Ga_xSe_2$ absorbers prepared by MBD two-stage process.

The average cell performance as shown in Table 5.8 indicated that our devices reach a maximum total area efficiency of 10.5% at a [Ga]/([In]+[Ga])= 0.5. Afterwards, it decreases with increase of Ga content. The loss in efficiency of $CuIn_{1-x}Ga_xSe_2$ solar cells with high Ga content is due to decrease in the fill factor and to a less extent V_{OC} caused by a drop in the photo-generated current with increasing forward bias voltage.

5.4.2 $CuIn_{1-x}Ga_xSe_2$ – based Thin Film Solar Cells: Absorber Grown by Three-stage Growth Process

As described in Chapter 2, NREL group [82] has used a three-stage process for the $CuIn_{1-x}Ga_xSe_2$ absorber preparation. In this recipe, the film starts without Cu atom, then goes through a Cu-rich phase at high temperature and then goes back to be a desired Cu-deficient (y=0.9) at the end of process. The $(In,Ga)_2Se_3$ precursors limit the depth of crevices. Then the intermediate Cu-rich phase helps in forming larger grains in the film, thus improving the performance of the absorber. In our research, the influence of [Ga]/([In]+[Ga])-ratios of $CuIn_{1-x}Ga_xSe_2$ absorber layer grown by three-stage process on solar cell performances was presented in Table 5.9.

Table 5.9: The average photovoltaic parameters of $CuIn_{1-x}Ga_xSe_2$ thin film solar cells with various x of absorber layers grown by three-stage process.

[Ga]/([In]+[Ga]) ratio	V_{OC} (mV)	J_{SC} (mA/cm^2)	FF (%)	η (%)	R_S (Ω cm^2)
0.0	488 ± 3	34.9 ± 1.1	63.9 ± 0.3	10.9 ± 0.7	2.3 ± 0.2
0.3	629 ± 1	32.5 ± 2.1	66.8 ± 0.5	13.7 ± 0.9	2.7 ± 0.1
0.5	641 ± 5	26.9 ± 4.0	63.9 ± 2.3	11.3 ± 1.3	3.7 ± 1.1
0.7	650 ± 5	27.7 ± 3.0	64.6 ± 0.7	11.6 ± 1.6	3.5 ± 0.2
1.0	740 ± 5	8.4 ± 0.5	56.1 ± 2.7	3.5 ± 0.3	11.2 ± 1.6

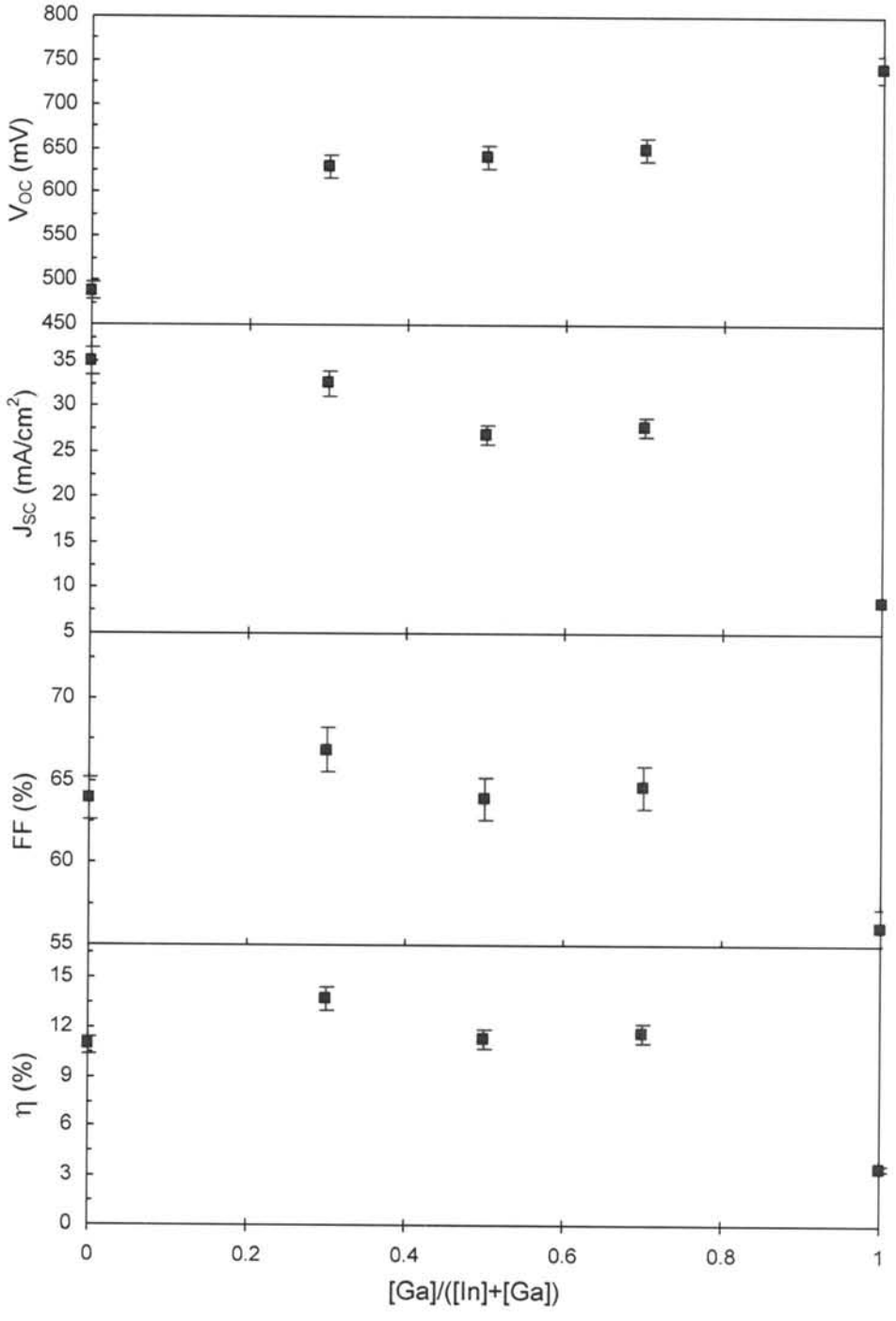

Figure 5.20: Average photovoltaic parameters of the Ni(Al)/ZnO/i-ZnO/CdS/ $CuIn_{1-x}Ga_xSe_2$/Mo/SLG solar cells with respect to the [Ga]/([In]+[Ga]) ratio based on as-grown $CuIn_{1-x}Ga_xSe_2$ absorbers prepared by MBD three-stage process.

Figure 5.20 shows that the $CuIn_{1-x}Ga_xSe_2$ solar cells fabricated from $CuIn_{1-x}Ga_xSe_2$ films with various x grown by three-stage growth process revealed that

the cell performance can be improved by using three-stage process. The high device-quality $CuIn_{1-x}Ga_xSe_2$ film with $x \leq 0.7$ can be fabricated to give the high performance solar cells. The V_{OC} values varied between 488 and 650 mV, J_{SC} values varied between 27 and 35 mA/cm^2, while the fill factor values were between 64 and 69%. Figure 5.21 shows the selected J-V characteristics of the $CuIn_{1-x}Ga_xSe_2$ solar cells fabricated from $CuIn_{1-x}Ga_xSe_2$ absorbers with various Ga contents grown by three-stage growth process. A trade-off between J_{SC} and V_{OC} in the J-V characteristics was also observed. A more detailed study is needed and is not included in this work. To date, we achieved the best cell (with an active area of $0.475cm^2$) with efficiency of 15.3% (without AR) as presented in Fig. 5.21.

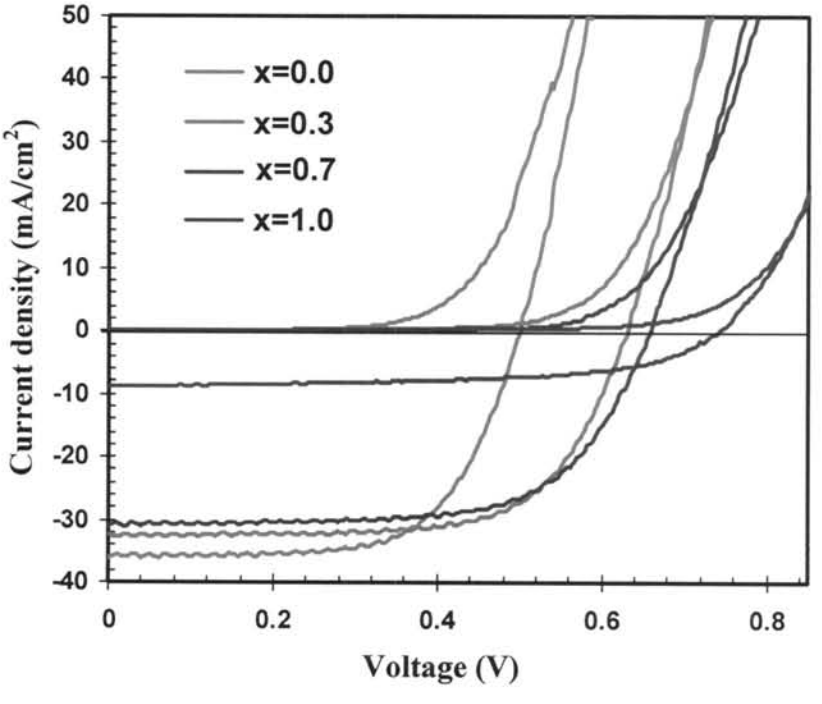

Figure 5.21: Selected J-V curves with various [Ga]/([In]+[Ga]) of $CuIn_{1-x}Ga_xSe_2$ films grown by three-stage process.

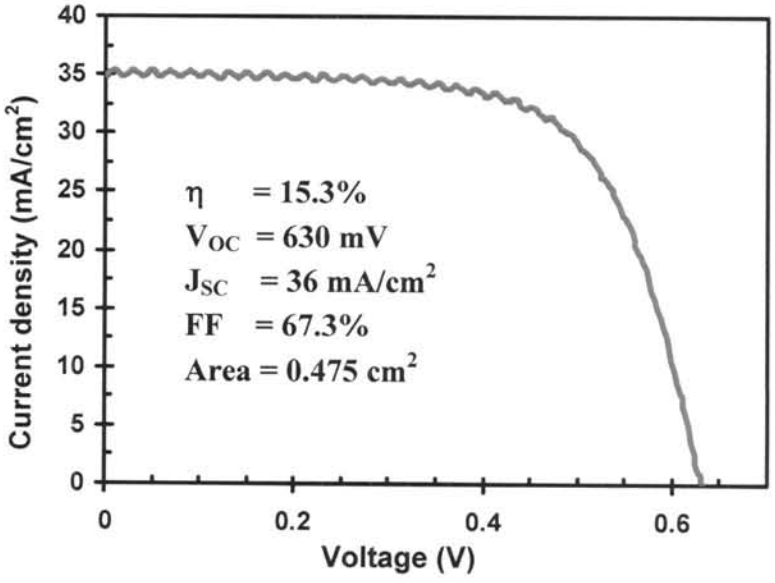

Figure 5.22: J-V curve of the best $CuIn_{1-x}Ga_xSe_2$ solar cell using the *in situ* monitoring in the three-stage process with x = 0.3.

5.4.3 Comparison of Cell Performances of the $CuIn_{1-x}Ga_xSe_2$ Thin Film Solar Cells Grown by Two-stage versus Three-stage Growth Processes

To compare the device-quality $CuIn_{1-x}Ga_xSe_2$ absorbers grown by two-stage versus three-stage growth processes, two sets of their average cell performances are plotted in the same charts as illustrated in Fig. 5.23. All photovoltaic parameters of the $CuIn_{1-x}Ga_xSe_2$ solar cells using the three-stage growth process to fabricate their absorbers are improved.

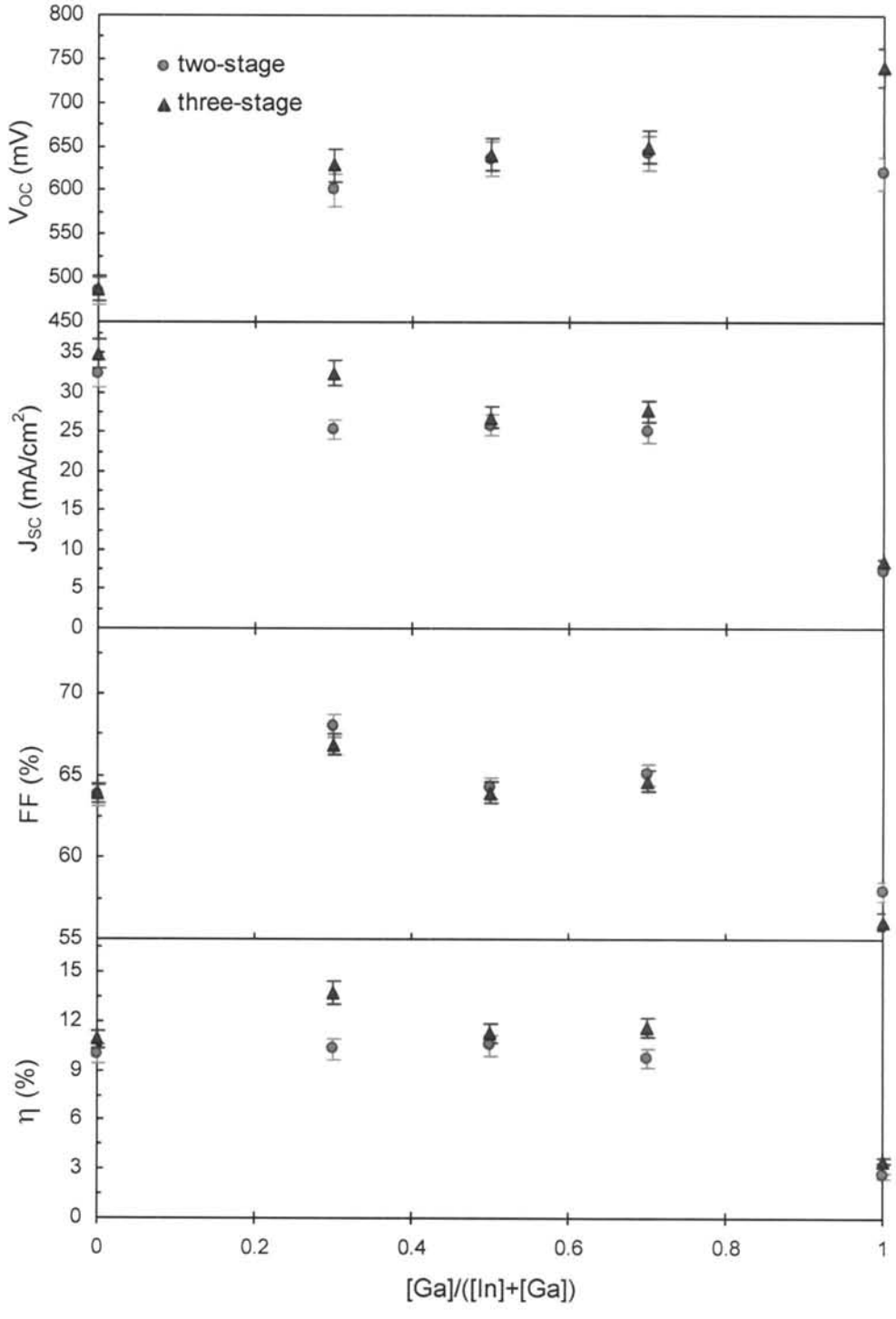

Figure 5.23: Comparison of the average photovoltaic parameters of $CuIn_{1-x}Ga_xSe_2$ thin film solar cells with $CuIn_{1-x}Ga_xSe_2$ absorber layers grown by two-stage versus three-stage processes.

To understand the highly increasing of V_{OC} value of the $CuGaSe_2$ device in Fig. 5.23, a plot of their best J-V characteristics of the $CuGaSe_2$ thin film solar cells is also presented in Fig. 5.24.

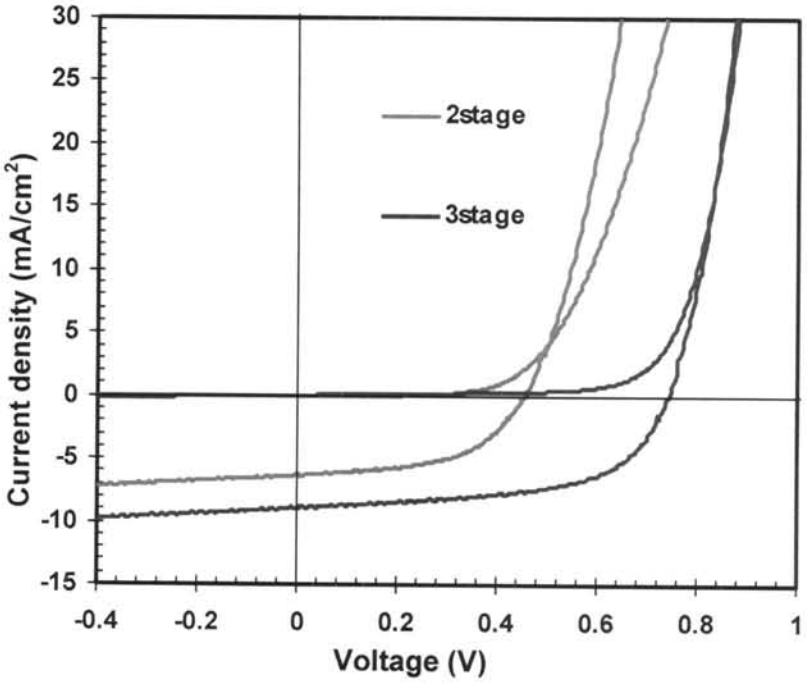

Figure 5.24: Comparison of J-V curves of $CuGaSe_2$ thin film solar cells with $CuGaSe_2$ absorber layers grown by two-stage versus three-stage processes.

The comparison of cell performances of the $CuGaSe_2$ thin film solar cells with $CuGaSe_2$ absorber layer grown by two-stage and three-stage process revealed that the J_{SC} up to 10 mA/cm^2 and FF up to 58% were obtained using the three-stage process. The improvement of V_{OC} was obtained. The values of V_{OC}, however, were limited to less than 750 mV. It is indicated that the V_{OC} of $CuGaSe_2$ thin film solar cells can be improved using the $CuGaSe_2$ absorber grown by three-stage process.

Figure 5.24 shows that the illuminated J-V of both two-stage and three-stage curves have a slight slope in the reverse bias region. This may be the result of poor

generated carrier improves, and the light-generated current slowly increases. It should be implied that when the reverse bias was increased, the depletion region extended more into the bulk of the absorber layer, thus, increasing the number of carriers that can reach the depletion region and be collected.

However, the J-V curves of $CuGaSe_2$ thin film solar cells with $CuGaSe_2$ absorber layer grown by two-stage process show a typical cross-over of the illuminated and dark curves, whereas the other curves show a simple diode characteristic except the V_{OC} value which remains lower than theoretical calculation. From the theoretical calculation, the V_{OC} of $CuGaSe_2$ thin film solar cell should be 1.2 V [83] with conversion efficiency of 26% [84, 85]. Recently, the V_{OC} of $CuGaSe_2$ thin film solar cells can be reached to 870 mV with modified surface of $CuGaSe_2$ films and highest conversion efficiency of 9.3% [86].

All of our $CuGaSe_2$ thin film solar cells had fill factor in the range of about 40-60% with high series resistance. Although all practical devices will always have some finite series resistance, the effect in our devices is rather large. The series resistance in solar cell generally comprise of bulk resistance of the absorber material, and any contact resistances. As the contacts used in this solar cell structure are highly conductive, the resistance is coming from the bulk of the absorber material itself.

In general, grain boundaries are potential recombination centers for photo-generated electron-hole pairs. This is due to high defect densities, impurity segregation, and carrier collecting fields often found at the grain boundaries. Furthermore, grain boundaries extending from top to bottom of the absorber film can be shunt paths and reducing the parallel resistance of the solar cells.

It can be suggested that the cell performances involved both the growth process of the absorbers and the solar cell fabrication process.